Measurements of the R-ratio in e^+e^- Annihilation at √<s>=55 and 56 GeV and a Search for New Heavy Quarks

AUTHOR(S):

Kurashige, Hisaya

Memoirs of the Faculty of Science, Kyoto University, Series of Physics, Astrophysics, Geophysics and Chemistry, Vol. XXXVIII, No. 1, Article 2, 1990

Measurements of the R-ratio in e^+e^- Annihilation at $\sqrt{s}=55$ and 56 GeV and a Search for New Heavy Quarks

By

Hisaya KURASHIGE

Department of Physics, Faculty of Science, Kyoto University

(*Received January 6, 1989*)

Abstract

We have measured the total hadronic cross section in e^+e^- annihilation using the VENUS detector at TRISTAN. The observed R-ratios are $R=4.11\pm0.30$ (statistical)±0.18 (systematic) at $\sqrt{s}=55$ GeV and $R=4.83\pm0.22$ (statistical)±0.21 (systematic) at $\sqrt{s}=56$ GeV. The present results are consistent with the predicted values of the known five flavor production obtained by the standard model. From the observed values, the weak mixing angle and the corresponding Z^0 mass are evaluated to be $\sin^2\theta_w=0.22\pm0.03$ and $m_z=93.0\pm5.0$ GeV/c^2. These values also agree with the world average values.

We have also searched for new heavy quarks by means of the detailed study of the event shape. There is no signs of the production of the heavy quarks. The lower mass limit of the top quark is 27.5 GeV/c^2 at 95% C.L. As for the b' quark which is a charge -1/3 quark of the fourth generation, the lower mass limit is 25.6 GeV/c^2 at 95% C.L.

1. Introduction

A modern theory of elementary particle physics, which is called "standard model", has enjoyed the great success to describe the interactions between elementary particles in the wide energy range from 10^6 eV to 10^{11} eV. According to the standard model, all matter consists of two families of point-like constituents, referred to as leptons and quarks. The leptons and quarks are spin 1/2 fermions and there are several species called flavors. They are classified as follows;

leptons: $\begin{pmatrix}\nu_e\\ e^-\end{pmatrix}$ $\begin{pmatrix}\nu_\mu\\ \mu^-\end{pmatrix}$ $\begin{pmatrix}\nu_\tau\\ \tau^-\end{pmatrix}$

quarks: $\begin{pmatrix}u\\ d\end{pmatrix}$ $\begin{pmatrix}c\\ s\end{pmatrix}$ $\begin{pmatrix}t\\ b\end{pmatrix}$

In 1975, the MARK I collaboration at SPEAR discovered the τ lepton in exotic events of $e^+e^-\to\mu e+$missing [1]. The advent of the τ lepton gave birth to the third generation and all 6 leptons of three generations were discovered up to now. On the quark family, a new particle called J/Ψ, which is now interpreted as a bound state of a charm quark and its antiquark, was discovered in 1974 [2]. The discovery of the charm quark completed the second generation and restored the lepton-quark symmetry. It was pointed out by Kobayashi and Maskawa [3] in 1973 that the existence of the third

generation could account for the CP violation phenomenon in terms of a quark mixing matrix of the weak interaction. The bottom quark, the third generation quark with a charge $-1/3$, was discovered at FNAL in 1978 [4] and was soon established by an experiment at DORIS [5]. The sixth quark (namely the top quark), however, has not been discovered experimentally. Thus, a search for the top quark is one of the major tasks of e^+e^- colliding experiments at high energies.

The elementary interactions between quarks and leptons are classified into three categories: the electromagnetic, the weak, and the strong interactions. In the standard model, all three interactions are explained by a principle referred to as a local gauge invariance. By basing on this gauge theory, both the electromagnetic and the weak interactions are unified in the electroweak theory established by Glashow, Weinberg and Salam [6]. The electromagnetic interactions between charged particles are mediated by a photon, which is related to a gauge group of $U(1)$. Similarly, the weak interactions are mediated by massive weak bosons of $W^{\pm}$ and Z^0, which are related to a gauge group of $SU(2)$. These weak bosons were actually discovered by CERN $\bar{p}p$ collider experiments in 1983 [7] and the observed masses of the weak bosons were consistent with the prediction of the minimal electroweak theory.

On the other hand, the strong interactions between hadrons are described by a gauge theory called the quantum chromodynamics (QCD). The QCD introduces a quantum number called a "color charge" which is associated to a $SU(3)$ gauge group. Each type of quarks has three colors and the force is mediated by massless gauge bosons named gluons which eonvey the color charge. The evidence of the existence of the gluon is indicated by various experimental results. The emission of the energetic gluon was clearly observed as a "three-jets" event at PETRA [8]. A detailed study on the "three-jets" events at PETRA [9] revealed that the gluon has a spin 1 and the cross section of gluon emission is consistent with the perturbative calculation by the QCD.

The most direct evidence that quarks have three colors comes from measurements of the total hadronic cross section in e^+e^- annihilation, i.e. $\sigma(e^+e^-\rightarrow\text{hadrons})$. For convenience, the total hadronic cross section is usually normalized by σ_{point} which is the QED lowest order point-like cross section of massless spin 1/2 particles of a unit charge. In the fermion pair production mediated by a photon, the total cross section is proportional to the square of its charge. Therefore, the normalized cross section R, which is defined as the ratio

$$R\equiv\frac{\sigma(e^+e^-\rightarrow\text{hadrons})}{\sigma_{\text{point}}},$$

is independent of the center-of-mass energy, and it is given by

$$R=3\sum_f Q_f^2,$$

where Q_f is the electric charge of the quark and f represents the produced quark flavor. The factor of 3 in the R-ratio originates from the number of quark colors, because quarks with different colors are produced impartially. For the production of known five flavors, namely u, d, s, c, and b quarks, the R-ratio is expected to be 11/3. Note that the

above expression of the R-ratio is a naive approximation. Precisely, it must include correction terms due to the Z^0 exchange and the gluon emission. At PETRA and PEP, the R-ratio has been measured by many groups [10, 11, 12] up to the $\sqrt{s}=47.2$ GeV. The measured values agree very well with the theoretical predictions by the standard model.

At the TRISTAN energies, the R-ratio is predicted to increase as the center-of-mass energy increases owing to the contribution of the Z^0 exchange. This contribution is expected to be about 20% and this term is sensitive to the Z^0 mass and the electroweak mixing angle. Therefore, precise measurements of the R-ratio give us much information on these fundamental parameters in the electroweak theory. The gluon emission also affects the R-ratio [13, 14], however this QCD correction is only about 5% and fortunately it is insensitive with respect to the center-of-mass energy.

A study on the hadronic production provides a straightforward way of a new heavy quark search in addition to the test of the standard model. Up to now, various experimental studies have imposed certain limits on the top quark mass. For example, a study on the $B^0\overline{B}^0$ mixing gives a lower limit, $m_t \geq 50$ GeV/c^2 [15]. Recently, UA1 group reported a lower mass limit of $m_t \geq 44$ GeV/c^2 by a study on the lepton production in the $\bar{p}p$ collider experiment [16]. The $B^0\overline{B}^0$ mixing, however, is not directly related to the existence of the top quark. Also the limit obtained by $\bar{p}p$ collider experiments is quite ambiguous because it involves a model dependent QCD calculation for the production rate of the heavy quarks. As for lower energy e^+e^- collider experiments, the PETRA groups observed no sign of the production of the top quark [11]. Thus, a search at TRISTAN is the best way to investigate the existence of new heavy quarks with small theoretical uncertainties and systematics.

About the fourth generation, no prediction exists in the standard model. A fourth generation quark with a charge $-1/3$, referred to as b' quark, may exist and may have a lower mass than that of the top quark. The PETRA groups have not observed any signs of the production of the b' quark [11], and UA1 group has reported a lower mass limit of $m_{b'} \geq 32$ GeV/c^2 [16].

This paper reports the measurements of the R-ratio at $\sqrt{s}=55.0$ GeV and 56.0 GeV using the VENUS detector at TRISTAN to provide the highest center-of-mass energies at present. The VENUS group also measured the R-ratio at $\sqrt{s}=50$ and 52 GeV [17]. The results of the measurements are then compared with the predictions of the standard model. The production of the top quark is also carefully tested. A search for new heavy quarks, the top quark and the b' quark, is also conducted using the 56 GeV data by the event shape analysis.

This paper is organized in the following way: Chapter 2 presents the description of the TRISTAN accelerator and the VENUS detector. Chapter 3 describes the selection criteria for hadronic events. Chapter 4 focuses on the theoretical backgrounds and analysis of the R-ratio in detail. A search for heavy quarks by means of the shape analysis is discussed in Chapter 5.

2. Experimental apparatus

The TRISTAN [18] is an e^+e^- colliding beam accelerator operated at the world highest energy on the KEK site in Tsukuba, Japan. Since the fall of 1987, TRISTAN was operated at the beam energy of 27.5 GeV and then at 28.0 GeV. In the spring of 1988, the peak luminosity amounted to $6\times10^{30}\,\mathrm{cm}^{-1}\mathrm{s}^{-1}$ and the average luminosity was $0.9\times10^{30}\,\mathrm{cm}^{-1}\mathrm{s}^{-1}$. The total integrated luminosity was $2.3\,\mathrm{pb}^{-1}$ at the center-of-mass energy of 55.0 GeV from October to December 1987 and was $5.3\,\mathrm{pb}^{-1}$ at 56.0 GeV from January to March 1988.

The VENUS detector [19] is a general purpose magnetic spectrometer built in the south-west experimental hall of the TRISTAN acceralator. The main feature of the VENUS detector is a large angular coverage for both charged and neutral particles with good momentum and energy resolutions. Especially, the electromagnetic calorimeters cover more than 99% of 4π without any gap. Figure 1 shows a side view of the VENUS detector. Inside the superconducting solenoidal magnet, the inner chamber, the central drift chamber and the outer drift tubes are installed to record trajectories of charged particles, and the time-of-flight counters are placed on the inner wall of the magnet. The end-cap liquid argon calorimeters and the luminosity monitors cover forward regions. The barrel streamer tubes and the barrel lead glass calorimeter are placed outside the magnet. Outside the magnet return yoke, the muon chamber system is installed. The outer drift tubes and the barrel streamer tubes were not used in this analysis. The forward parts of the muon chambers, the transition radiation detector, and the superconducting quadrupole magnets (QCS) had not been installed yet in the 55 and 56 GeV runs.

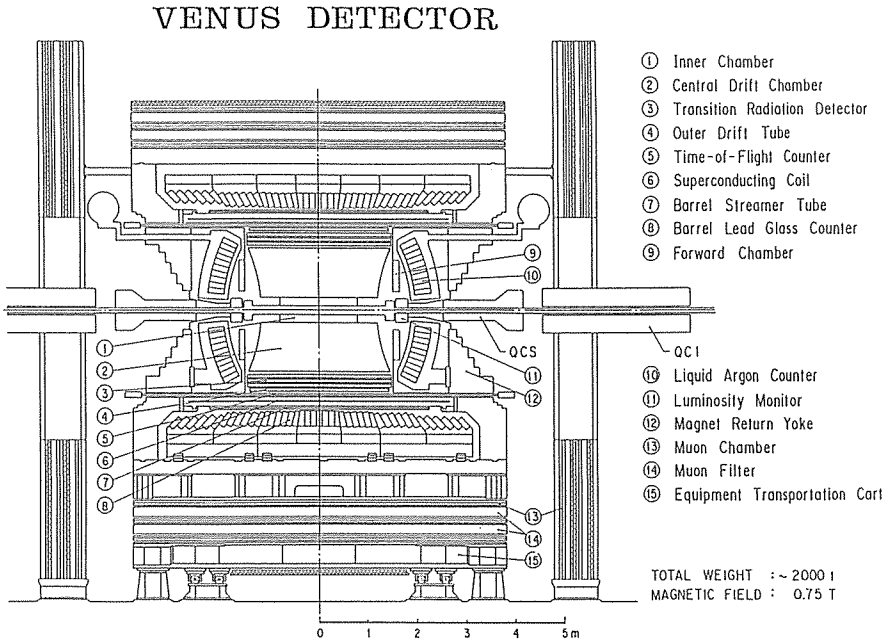

Figure 1 Side view of the VENUS detector.

2.1. *Beam pipe and luminosity monitor*

The beam pipe made of aluminum has an inner radius of 90 mm at the central region of $|Z|<135$ cm. In the interaction region of $|Z|<25$ cm, the thickness of the beam pipe is chosen to be 2.5 mm to minimize the multiple Coulomb scattering and the photon conversion. A pair of vacuum ion chambers is placed at both sides of the central region so that the vacuum at the interaction point is kept below 10^{-8} Torr.

In order to measure small angle Bhabha events, a pair of luminosity monitors (LM) [20] is placed surrounding the beam pipe at 155 cm apart from the interaction point in both sides. In the summer of 1987, the luminosity monitors were replaced with new ones since the beam pipe was enlarged in radius at the region of the luminosity monitors. Each new luminosity monitor consists of 27 alternating layers of lead sheets and plastic scintillators corresponding to 20 radiation lengths in total. It is divided into 8 sectors in the r-ϕ plane. The inner and outer radii are 12 and 24 cm, respectively. The angular coverage is between 76 and 137 mrad. Scintillation lights are guided to wavelength shifters through inner and outer edges of the scintillators, and then are transmitted to the mesh type photomultiplier tubers (HAMAMATSU R2490) which can be operated in the magnetic field of 7.5 KGauss.

Pule heights of phototube signals are measured by the charge sensitive ADC's (LeCroy 1885) on FASTBUS. By using the pulse height information from the inner and the outer sides, the radius of the hit position of an electron and/or a photon is measured as well as its energy. The energy resolution is $\delta E/E=15\%/\sqrt{E}$, where E is the shower energy in units of GeV.

2.2. *Inner chamber*

The inner chamber is designed as a Z-trigger chamber making use of the hit information of the cathode pads. The Z-trigger system of the inner chamber was completed in the trigger scheme of the VENUS detector in the summer of 1988. During the 55 and 56 GeV runs in the winter of 1987–1988, the information of the Z-trigger system was used in the "Process 1" as described in Chapter 3.

The inner chamber is a cylindrical drift chamber of 6 layers with segmented cathode pads; the inner and outer radii are 10 and 24 cm, respectively, and the total length is 160 cm. It covers the whole azimuthal angle of ϕ and the polar angle of $|\cos\theta|$ <0.96. An r-θ view of the inner chamber are shown in Figure 2. 7 layers of paper core honeycomb cylinders of 6 mm and 18 mm thick form the chamber structure and support the endplates made of 12 mm thick aluminum.

The inner chamber has 640 drift cells and the each cell size is about 1×1 cm^2. The chamber is filled with HRS gas ($Ar:Co_2:CH_4=89:10:1$) at a pressure of 1 atm. The anode wires of 30 μm in diameter are made of gold plated tungsten and a positive high voltage is applied to them. The potential wires of 120 μm in diameter are made of an alloy of copper and beryllium and they are grounded. Two cathode planes of each layer are segmented into 16 in the z derection and 8 in the ϕ direction. The corresponding pad of each layer is designed to cover the same solid angle from the interaction point as shown in Figure 3. In this manner, cathode pads are formed into 128 towers of 6 layers.

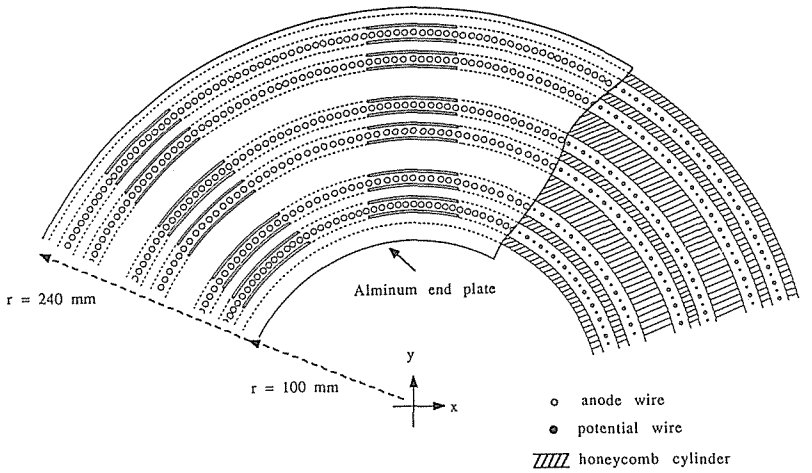

Figure 2 Part of the r-θ view of the inner chamber endplate. The left half side of the figure shows the aluminum endplate. Here, the circles are the holes for supporting the wires. The right half side shows the chamber structure, where the circles and the dashed area indicate the wires and the honecomb cylinder, respectively.

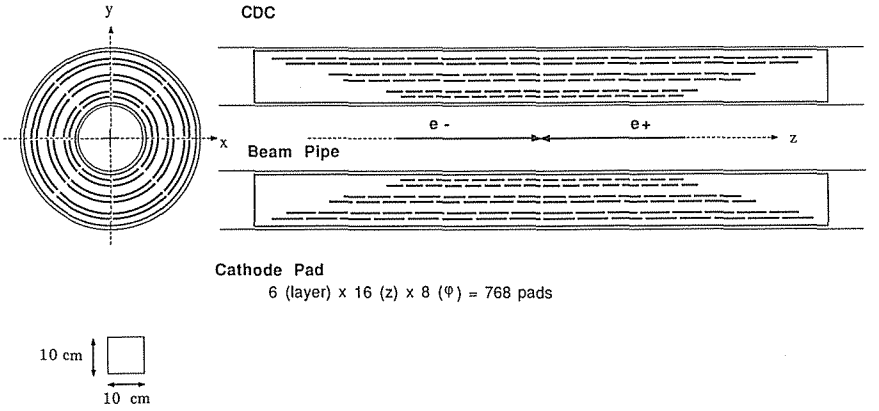

Figure 3 Configuration of the cathode pads of the inner chamber. The bold lines indicate cathode pads of each layer.

Each cathode pads consists of arrays of fine copper lines (18 μm thick and 1.0 mm wide) printed on Kapton sheets of 125 μm thick which are glued onto the honeycomb cylinders. The typical printed pattern of the cathode pads is shown in Figure 4. The use of very thin cathode pads and honeycomb cylinders reduces the materials of the chamber and the total thickness of the chamber material is equivalent to 0.03 radiation lengths along the direction perpendicular to the beam axis. The cathode plane of outer side of each layer is grounded. Signals of the inner side are sent out through readout lines printed on the other surface of the Kapton sheet. The total number of readout channels are 768 for the cathode pads. Innermost and outermost surfaces of the chamber are covered by thin copper planes on Kapton sheets and they are grounded in

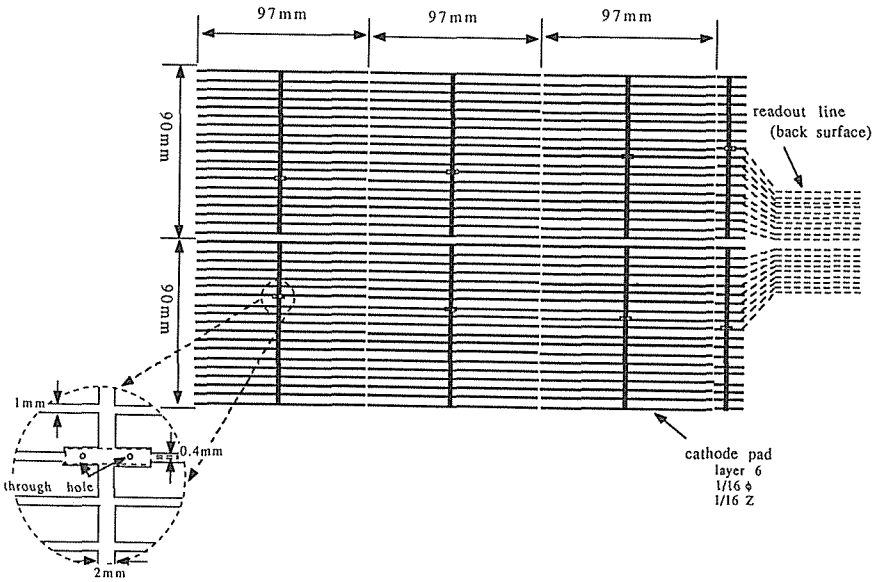

Figure 4 Part of the cathode pad layout pattern of the outermost layer of the inner chamber.

order to shield the chamber electrically. Details of the inner chamber can be seen in the reference [21].

Signals from anode wires are amplified by the preamplifiers [22] mounted on the endplate, and then the amplified signals are sent to the electronics hut through 37 m long doubly shielded 19-pair twisted cables in quasi-differential mode. The signal lines are connected through the pulse transformer in order to isolate the chamber electrically. Post-amplifiers of the gain 10 (Plessy SL560C) and discriminators (LeCroy MVL407) are installed in the electronics hut. The output signals from the discriminators are sent to the TDC system [23] on FASTBUS. These scheme for measurements of the drift time are almost the same as that used for the central drift chamber. The spatial resolution is about 350 μm for each wire. This resolution is restricted by the threshold voltage of the discriminators, which is set rather high to avoid noise pick-up. The information from the inner chamber was not used to reconstruct charged tracks in this analysis.

Signals from the cathode pads are amplified by the preamplifiers mounted on the endplates. Figure 5 shows the circuit diagram of the preamplifiers used for the cathode signals. A common base configuration followed by two stages of emitter followers without overall feedback is adopted for this preamplifier. The gain of the preamplifier is 200 mV/pC and the rise time and the fall time are 30 nsec and 200 nsec, respectively. The amplified signals are sent to the electronics hut through 37 m long doubly shielded 19-pair twisted cables in quasi-differential mode. Then, the signals are fed into the post-amplifier and discriminator modules on TKO boxes [24]. The post-amplifier is an amplifier of the pulse shaping type with four-stage semi-gaussian integrators of the gain of 30 dB. This pulse shaping reduces pick-up noises and cross-talk signals between adjacent pads. Since lines of the cathode pads and readout lines go in parallel on each

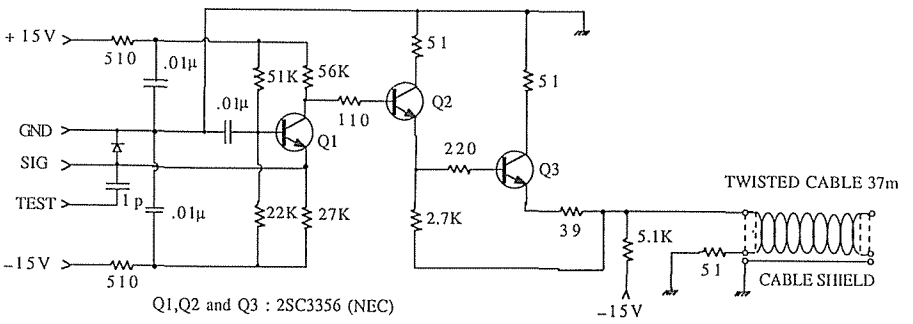

Figure 5 Circuit diagram of the preamplifier for the cathode pads of the inner chamber.

surface of the same kapton sheet, the cross-talk signals are induced by a capacitive coupling between them. Output signals are discriminated at the threshold voltage of 50 mV. A hit pattern of the discriminator is sent to the track-finding processor on FASTBUS.

The cathode pads are segmented into 128 towers of 6 layers. A charged particle originated from the interaction point will give six hits in one tower where the particle passes through. Therefore, as a criterion for track finding in the inner chamber, at least five hits in a tower are required. In order to avoid inefficiency due to gaps between the towers, two adjacent pads in the z direction are combined to search a charged track. The inner chamber has been operated at the positive high voltage of 1700 V and efficiency at 1700 V is found to be 99.5%. For this case, the trigger inefficiency of the inner chamber is estimated to be less than 10^{-3}. The look-up table method by using static RAMs is employed for fast track finding. The fast track-finding processor for the inner chamber is the same type as that for the central drift chamber [25]. The hit patterns of the cathode pads which should be accepted are loaded through FASTBUS. Dead channels are regarded as hit channels in order to avoid the inefficiency.

The information of the track-finding processor for the inner chamber has been used for the coplanar trigger which appears in Section 2.9 from the 57 GeV run in the summer of 1988. The following conditions are required for the events accepted by the coplanar trigger: For each track found in the central drift chamber, at least one hit tower of the inner chamber is required in the corresponding ϕ region. By using the Z-trigger system of the inner chamber, the trigger rate of the coplanar trigger can be reduced to about 1/3 of the rate without the Z-trigger. The reduction ratio changes accordingly as the beam condition changes. Figure 6 indicates how effectively the Z-trigger works. In fact, Figure 6 (a) shows a scatter plot in $\cos\theta$ and $Z_{\min}$ of the tracks for the events accepted by the coplanar trigger without the Z-trigger. This plot indicates an acceptance of the central drift chamber. Whereas Figure 6 (b) shows the same scatter plot for the events accepted by the coplanar trigger plus the Z-trigger. These figures show that the tracks with large $Z_{\min}$ are rejected and the tracks originated from the interaction point remain after the Z-trigger.

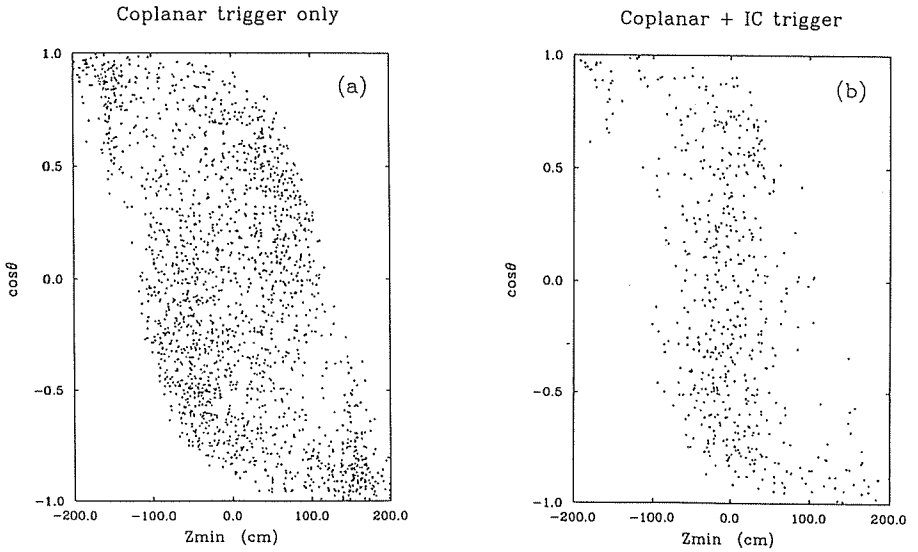

Figure 6 Scatter plots in $\cos\theta$ and $Z_{\min}$ of the charaged tracks for the events accepted by the coplanar trigger without the Z-trigger (a) and for the events accepted by the coplanar trigger with the Z-trigger (b).

2.3. *Central drift chamber*

The central drift chamber (CDC) [26] is a cylindrical drift chamber, which is the main tracking device of the VENUS detector. The dimension is 300 cm long with inner and outer radii of 25 and 126 cm, respectively. It consists of 20 layers of axial wires parallel to the beam axis and 9 layers of slant wires at the angle of $\pm 3.5^\circ$. The chamber is filled with HRS gas at a pressure of 1 atm. The details of the electronics were reported elsewhere [22, 23].

For charged tracks in the range of $|\cos\theta| < 0.75$, 20 r-ϕ and 9 r-z coordinates are measured. The mean spatial resolution is 270 μm at each axial layer. The momentum resolution of charged particles in the plane transverse to the beam axis is $[\delta P_t/P_t]^2 = [0.8\% \times P_t]^2 + [1.3\%]^2$ at B=7.5 KGauss, where P_t is a transverse momentum in units of GeV/c. The angular resolution in azimuthal and polar angles for the charged particles of high momenta are $\sigma_\phi \simeq 1.3$ mrad and $\sigma_\theta \simeq 9 \times \sin^2\theta$ mrad, respectively. The charged tracks which have the transverse momentum of larger than 0.7 GeV/c within the polar angle range of $|\cos\theta| < 0.87$ are searched in the r-ϕ plane by using the fast track-finding processors [25] on FASTBUS for the charged track triggers.

2.4. *Time-of-flight counters*

The time-of-flight counter system (TOF) [27] consists of 96 plastic scintillators (KYOWA SCSN-23) of 466 cm long surrounding the central drift chamber at a radius of 1.66 m. Details of the time-of-flight system are described in Appendix.

The time-of-flight of each charged particle is calculated by using information from phototubes on both sides of the counter. The timing resolution is 200 psec for Bhabha

and μ-pair events. Hit infromations of the time--flight counters are used for the charged track triggers.

2.5. *Superconducting solenoidal magnet*

The superconducting solenoidal magnet provides a uniform magnetic field of 7.5 KGauss in the direction of the z axis. The dimensions of the magnet are 3.4 m in diameter and 5.2 m in length. The magnetic field was measured before detector installation and was sufficiently uniform within 1% throughout the tracking volume. Details of the solenoidal magnet are described elsewhere [28].

2.6. *Barrel lead glass calorimeter*

The barrel electromagnetic calorimeter (LG) [29] comprising 5160 lead glass modules is located outside the solenoid for measuring energies of photons and electrons. It has an angular coverage of $|\cos\theta|<0.80$ and is divided into 120 segments in the ϕ direction and 43 segments in the z direction. The lead glass modules are placed in a semi-tower geometry; each module points toward the interaction point but not exactly. It tilts at small angle in both ϕ and z directions in order to avoid the large shower leakage along inter-module gaps. This configuration reduces the probability of multiple hits in the same lead glass module. The lead glass modules are made of NIKON DF6 with a refraction index of 1.8. Its typical size is 12.0×11.6 cm^2 in cross section and 30 cm in length corresponding to 18 radiation lengths ($1X_0=1.7$ cm). A phototube (HAMAMATSU R1911, R1652) surrounded by a μ-metal magnetic shield is mounted on each module together with a plastic light guide of 5 cm long. For monitoring the gain variation of phototubes, light pulses from Xenon flash tubes is distributed to each phototube through optical fibers. Two identical monitoring system are provided for cross-check.

Signals from phototubes are sent to the 96 channel charge integrating ADC modules (LeCroy 1885) on FASTBUS through RG174/u coaxial cables. The ADC has a 12-bit resolution and a 15-bit dynamic range by means of automatic selection between high and low ranges. For the energy trigger, the lead glass calorimeter is grouped into 58 segments: 7 segments in the z direction and 8 (or 10) segments in the ϕ direction. Analog signals in each ADC module corresponding to one segment of the calorimeter are summed up into one segment-sum signal. Each segment-sum signal is sent to a discriminator and its output signal is used for the segment-sum trigger. Moreover, all 58 segment-sum signals are sent to an analog-sum circuit in order to obtain the total energy deposit in the barrel calorimeter, which is used for the total-energy trigger.

The energy resolution is $\delta E/E=3.8\%$ and the angular resolutions of shower center are $\sigma_\phi=4$ mrad and $\sigma_\theta=4$ mrad for Bhabha events at $E=28$ GeV.

2.7. *End-cap light argon calorimeter*

At each side of the forward region in the VENUS detector, the endcap liquid argon calorimenter (LA) is installed as an electromagnetic calorimeter between the central drift chamber and the end-cap return yoke. Since the 55 GeV run in October 1987, the end-cap liquid argon calorimeters came into operation. Each calorimeter comprising 480

tower modules covers an angular range of $0.79<|\cos\theta|<0.99$; thus there is no energy leakage gaps between the endcap and the barrel calorimeters. Each tower module consisting of 71 calcium-lead plates of 1.5 mm thick (20.3 X_0) looks at the point 79 cm away from the interaction point on the beam axis. Each calorimeter is filled with liquid argon of 86°K.

Lead plates of each module are elecrically segmented into 4 groups. Accordingly, each side of the calorimeters has 1920 channels of signal readouts. Signals are amplified by the preamplifiers placed directly on the outer vessel of each calorimeter and then sent to the electronics hut through twisted pair cables. Signals from the preamplfiers are processed by the shaper amplifiers and pulse heights are measured by the sample-hold ADCs on TKO boxes. Two types of energy sum triggers are provided using the analog sum circuits for the end-cap calorimeters. Each calorimeter is divided into 12 sectors and each sector is further divided into the inner part ($0.91<|\cos\theta|<0.99$) and the outer part ($0.79<|\cos\theta|<0.91$). Thus energy sum signals of each subsector provide a total of 24 sector sum triggers. Furthermore, the total sum signal of all 1920 channels for each side is also provided.

The energy resolution is $\delta E/E=3.5\%$ and the angular resolutions of shower center are $\sigma_\phi=6$ mrad and $\sigma_\theta=4$ mrad for Bhabha events at $E=28$ Gev.

2.8. *Barrel muon chamber*

The barrel muon detector (MU) [30] consists of four layered arrays of 8-cell drift tubes made of extruded aluminum, which are located outside of the return yoke (30 cm thick iron). Three layers of drift tubes are interleaved with 20 cm thick iron filters. They measure the r-ϕ positions. The outermost layer of tubes is placed directly on the third layer without any iron filters. It measures the z-positions. Each 8-cell drift tube of 7.6 m long consists of 2 layers of 4 cells staggered by a half cell. Each cell has a cross section of 7×5 cm^2. The wires of 70 μm in diameter is made of gold plated tungsten with 3% of rhenium. The tubes are filled with P10 gas ($Ar:CH_4=90:10$) at a pressure of 1 atm. The coverage of solid angle is 62% of 4π and the total number of tubes is 3118.

Drift times of all channels are digitized by the front-end electronics comprising amplifiers, discriminators, and 6bit-TDCs with 40 MHz clock, which is mounted at one end of tubes. Digitized data are sent to the memory modules on TKO boxes in the electronics hut together with the wire address information. The spatial resolution is about 1 mm.

By combining information of this muon chamber system and tracking information of the central drift chamber, muons of larger than 2.3 GeV/c are identified with a detection efficiency of about 92%.

2.9. *Event trigger*

There are two types of event triggers in the VENUS trigger system [31]: neutral triggers based on the information of energies from the calorimeters and charged track triggers based on the information from the central drift chamber. The conditions for the neutral triggers are as follows:

1) Lead glass calorimeter total energy trigger:
Total energy deposits in the barrel lead glass calorimeter is larger than 5 GeV;

2) Liquid argon calorimeter total energy trigger:
At least one side of the end-cap liquid argon calorimeter has total energy deposits of larger than 6 GeV;

3) Liquid argon calorimeter sector sum trigger:
Total energy deposits in one sector of the liquid argon calorimeter is larger than 2.5 GeV.

On the other hand, the conditions of charged track triggers are as follows:

4) Coplanar trigger:
At least one pair of tracks in a back-to-back configuration is found by the track finder of the central drift chamber. An angle between these two tracks is larger than 170° in the r-ϕ plane and associated hits in the TOF counter are required for both tracks;

5) Lead glass calorimeter segment sum trigger:
At least two tracks is found by the track finder of the central drift chamber. In addition, at least one of the lead glass calorimeter segments have energy deposits of larger than 0.7 GeV.

In addition, an energy trigger by using the information of the luminosity monitor is provided for Bhabha events in the small angle regions. However, the events accepted by only this luminosity trigger were not used for this analysis.

The trigger rate was 3 Hz on average and the charged track trigger was about 60% of total events. But the rate of each trigger strongly depends on the beam condition.

2.10. Data acquisition system

The data acquisition system of the VENUS detector [32] employs the separated data bus system; relatively simple and cost effective "front-end bus" for signal processing of the front-end electronics, and a more sophisticated but expensive "online bus" for the complicated data manipulation. This system enables us to choose various configurations of front-end electronics systems which are suitable to each detector part.

For the fron-end bus, several simple data buses such as CAMAC, TKO bus, and simple analog buses are used. The front-end electronics usually requires straight forward data handling such as analog to digital conversions, pedestal subtractions, and data compressions by zero suppression. These buses handle about 25000 electronic channels of readout in total. In order to handle such a large number of electronic channels quickly, the parallel processing is adopted on the front-end bus. For each part of the detector, the signal processing such as sample-and-hold operations and A/D conversions are performed in parallel. The data size is compressed after the pedestal subtraction by zero suppression . A typical data size for whole detector system is thus limited to be about 1500 words. Many types of interface modules which depend on the type of the fron-end bus are used. These interface modules are the modules which

connect the front-end bus with the online bus. FASTBUS is adopted as the online bus through which the data from each detector part are transferred to the online computer. Since FASTBUS has high data transfer speed and flexible protocol, the data acquisition can have a large flexibility for the system configuration.

The online computer VAX11/780 readout the event data whenever event triggers occurs. It takes about 30 msec to readout all the data word for the event. The dead time is typically 10%. The collected data are transferred to the main frame computer, FACOM M382 (replaced by M780 in April '88), via optical link and then stored on the automatic loading cartridge tape library. Collected data are sampled by VAX11/780 and the selected data are transferred to the another online computer VAX8530. All the events send to the VAX8530 are quickly analyzed to check the run status.

The VENUS data acquisition system has a special feature called "fast clear scheme". Since the beam crossing occurs every 5 μsec, sample-and-hold of front-end analog signals and/or A/D conversion are performed for every beam crossing. If any event trigger conditions are not satisfied, a fast clear signal is generated 800 nsec before the next beam crossing. By receiving the fast clear signal, all front-end modules reset their sample-and-hold circuits and are ready for next events. If the trigger conditions are satisfied, analog to digital conversion for sample-and-hold signals, data compression, and data transfer proceed. This scheme is successful to remove any expensive signal delay lines for the front-end electronics, although the short time interval for signal processing in this scheme forces the front-end electronics in hard operating conditions.

3. Selection of the hadronic events

The hadronic events was selected in two steps. At the first step, background events which were not originated from e^+e^- interaction were rejected. This procedure was called "Process 1". The reconstruction of charged tracks and the calorimeter calibration were performed in this step. At the second step, stringent selection criteria were applied to select multihadronic events.

In this analysis, a right-hand coordinate system is adopted; the z axis points along the electron beam, and the y axis points upward along a vertical line. The origin is chosen to be the center of the VENUS detector where e^+e^- collisions are expected to occur.

3.1. Process 1

At first, a preselection was performed for the events accepted by the charged track triggers. The purpose of this preselection was to reject the events which had no track originated from the interaction point without the reconstruction of charged tracks in the central drift chamber. The vertex positions of any charged particles were examined in the r-z plane by using the hit information of cathode pads of the inner chamber. More than 4 layer hits out of 6 layers of an associated tower were required for all charged tracks found by the track finder of the central drift chamber. Unless an associated hit tower was found in the inner chamber, the track was treated as a fake track. Tracks with a vertex apart from the interaction point in the r-z plane could be rejected by

requiring the hit tower. Then, the trigger conditions were examined; a pair of back-to-back tracks were required for the events accepted by the coplanar trigger and at least two tracks were required for the events accepted by the LG segment trigger. Events were rejected if neeither trigger conditions were satisfied. About 50% of the events accepted by only the charged track triggers were rejected by this preselection. All the events accepted by a neutral trigger were sent to the next stage without this preselection.

Next, the tracks of charged particles were reconstructed by using the information of the central drift chamber [33]. The reconstruction efficiency was larger than 89% and 99% for charged particles in the polar angle range of $|\cos\theta|<0.9$ and $|\cos\theta|<0.75$, respectively, if the track is isolated from other tracks. The energy calibration and the clustering of shower energy deposits for the barrel and end-cap calorimeters were performed, so that the energy and the direction of electrons and/or photons were reconstructed. Then, several criteria were applied to select the real events originated from the e^+e^- interaction. If at least one of the following requirements were satisfied, the events were accepted.

1) Total shower energy deposited in the barrel calorimeter was larger than 3.0 GeV for the event accepted by the LG total energy trigger.

2) Total shower energy deposited in the end-cap calorimeters was larger than 3.0 GeV for the event accepted by the LA total energy trigger.

3) Total shower energy deposited in the end-cap calorimeters was larger than 1.5 GeV for the event accepted by the LA sector sum trigger.

4) At least two "long tracks" were detected in the central drift chamber for the event accepted by the coplanar trigger.

5) At least one "long track" was detected in the central drift chamber and the total energy of the barrel calorimeter was larger than 0.5 GeV for the event accepted by the LG segment sum trigger.

Here, the reconstructed track was accepted as a "long track", if it satisfied the following requirements:

(a) The track was reconstructed in both r-ϕ and r-z planes with more than 9 axial wire hits and more than 3 slant wire hits.

(b) The radial distance of the closest approach of the track to the origin in the r-ϕ plane, $R_{\min}$, and the z-coordinate of this point, $Z_{\min}$, were within $|R_{\min}|<7$ cm and $|Z_{\min}|<30$ cm, respectively. The $R_{\min}$ is defined to be positive if the origin was inside in the circle of the track.

(c) The transverse momentum to the beam axis was larger than 0.2 GeV/c.

The reduction ratio of the "Process 1" depends on the beam condition. The remained events was about 35% of all triggered events on an average. At 56 GeV, 1.9 million events satisfied "Process 1" out of 4.8 million total triggered events. The number of trigger events and accepted events are listed in Table 1.

Table 1. Number of events at each step in the selection

	55 GeV	56 GeV
Total number of triggers	3,613,512	4,815,174
Process 1	1,228,871	1,861,294
Selection criterion (1)	151,451	196,777
Selection criterion (2)	378	943
Selection criterion (3)	378	936
Selection criterion (4)	340	846
Selection criterion (5)	319	803
Selection criterion (6)	274	681
Selection criterion (7)	211	507

3.2. Hadron selection

The selection criteria for multihadronic events are optimized in order to minimize any background contamination: Bhabha scattering events, two-photon events, τ-pair events, and other background events. These background events have low charged multiplicities and/or small energy deposits on the calorimteres in comparison with multihadronic events. Therefore, the following criteria were applied in order to reduce these background.

At first, background events with small energy deposits were eliminated by the following calorimeter energy cut.

(1) Total energy deposit in the calorimeter, $E_{\rm cal}$, was larger than 5 GeV.

The $E_{\rm cal}$ is defined as a sum of the shower energy deposits in the barrel calorimeter and those in outer parts of the end-cap calorimeters on both sides ($|\cos\theta|<0.91$). The energy deposit in inner parts of the end-cap calorimeters is excluded in $E_{\rm cal}$ because of the poor tracking capability in this region. The most of the events fall into the region of $E_{\rm cal}<3$ GeV, so that about 90% of the total events were rejected by this $E_{\rm cal}$ cut. Most of these rejected events were two photon events and cosmic ray events with two coplanar tracks.

Next, the number of charged tracks which were well reconstructed in the central drift chamber was tested. The track satisfying the following requirements was accepted as "good track":

(a) The track could be reconstructed in both r-ϕ and r-z planes with more than 7 axial wire hits and more than hits in slant wires of the central drift chamber.

(b) The transverse momentum was larger than 0.2 GeV/c and the polar angle was within the range of $|\cos\theta|<0.85$.

(c) The $R_{\rm min}$, and the $Z_{\rm min}$, of the track were within $|R_{\rm min}|<2$ cm and $|Z_{\rm min}|<20$ cm, respectively.

The last criterion (c) was effective to reduce fake tracks. Also, the tracks originated from beam-beam pipe interactions and photon conversions in the detector were effec-

tively rejected by this criterion. The distributions of the vertex have a sharp peak at the origin for the real track so that these cut values are chosen to be sufficiently safe.

The second selection criterion for the hadronic events was;

(2) At least 5 good tracks were detected in the central drift chamber.

The number of good tracks required in the selection criterion (2) was chosen to reduce τ-pair events, since most of τ-pair events have two or four charged tracks.

Most of Bhabha events have only two charged tracks and so they can be rejected by the criterion (2). But, some of Bhabha events have charged tracks originating from electromagnetic showers produced at the beam pipe. Such events may have more than four charge tracks in total. The Bhabha events are characterized by the large calorimeter energy deposits which are nearly equal to $2\times E_{\text{beam}}$. Therefore, in order to eliminate the Bhabha events, the selection criteria for the total calorimeter energy E_{cal} was set as follows;

(3) Total calorimeter energy, E_{cal}, was smaller than $1.8\times E_{\text{beam}}$.

To set the fourth selection criterion, the invariant mass was calculated for observed particles in each hemisphere divided by the plane perpendicular to the thrust axis. Here, the thrust, T, is defined by

$$T=\max_{\boldsymbol{e}_T}\left\{\frac{\Sigma\,(\boldsymbol{P}^i\cdot\boldsymbol{e}_T)}{\Sigma\,|\boldsymbol{P}^i|}\right\},$$

where the maximum is found by varying the direction of the unit vector, $\boldsymbol{e}_T$, the direction of which is defined as the thrust axis. The summation is extended over all good tracks and all clusters with energies of larger than 0.2 GeV. The thrust axis points along the direction of initial quarks for the two-jets events. In the calculation of the invariant mass, each charged track in the hemisphere is assumed to be a pion track and its energy is calculated by using its observed momentum and pion mass. Whereas, each shower cluster in the calorimeters is assumed to be a photon shower and its momentum is calculated by using observed cluster energy and position.

This selection criterion was as follows:

(4) The invariant mass of observed particles in each hemisphere divided by the plane perpendicular to the thrust axis was larger than 2 GeV/c^2.

The invariant mass is called a jet mass and it indicates generally the mass of the initial particle of the jet in the hemisphere. This cut was also quite effective to reduce τ-pair events and Bhabha events.

Finally, there remained 340 events at $\sqrt{s}=55$ GeV and 846 events at 56 GeV after applying the selection criteria (1), (2), (3), and (4). The multihadronic events produced by one photon/Z^0 annihilation are characterized by a large total visible energy and a small missing momentum along the beam direction. The total visible energy, E_{vis}, and the longitudinal momentum balance, P_{bal}, are defined as follows:

$$E_{\text{vis}}=\Sigma\,E_{\text{cl}}+\Sigma\,p_{\text{trk}}\quad\text{and}\quad P_{\text{bal}}=[\Sigma\,E_{\text{clZ}}+\Sigma\,P_{\text{trkZ}}]/E_{\text{vis}}\,.$$

Here, E_{cl} is the cluster energy deposited in the calorimeters and P_{trk} is the momentum of a charged particle observed in the central drift chamber. E_{clZ} and P_{trkZ} are the z-components of E_{cl} and P_{trk}, respectively. The summation is extended over all good tracks and all clusters in both the barrel and the end-cap calorimeters. Figure 7 shows the distributions of E_{vis}/E_{beam} (a) and P_{bal} (b) together with the result of Monte Carlo simulations of the multihadronic events. The Monte Carlo calculation simulates responses of the VENUS detector for hypothetical multihadronic events. As shown in Figure 7 (b), the distribution of E_{vis} for multihadronic events have a broad peak at about $2\times E_{beam}=\sqrt{s}$, whereas background events have a smaller peak at lower visible energies because most of those are two-photon events.

The following criteria were applied to the events accepted by the selection criteria (1), (2), (3), and (4);

(5) The absolute value of the longitudinal momentum balance, $|P_{bal}|$, was less than 0.4.

(6) The total visible energy, E_{vis}, was larger than the beam energy.

This visible energy cut was most effective to reduce two-photon events. There remained 274 events at $\sqrt{s}=55$ GeV and 681 events at 56 GeV. as candidates of the multihadronic events, respectively. These multihadronic candidates were used to evaluate the R-ratio which appears in Chapter 4.

For a detailed study of the event shape, a further selection criterion was applied to the multihadron candidates selected above. The charged particles can be accepted as good tracks in the range of $|\cos\theta|<0.85$. Then, the reconstruction efficiency of charged tracks in a jet becomes worse as the direction of the jet going forward. In order to ensure that most of final particles were inside the fiducial volume of the central drift chamber, the following selection criterion was required:

(7) The polar angle of the thrust axis was within $|\cos\theta_T|<0.7$.

By this selection criterion about 25% of multihadronic candidates were cut out. There remained 211 events at $\sqrt{s}=55$ GeV and 507 events at 56 GeV, respectively. Table 1

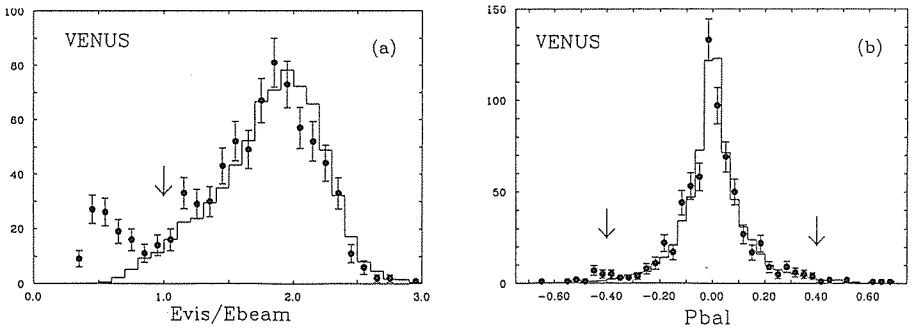

Figure 7 Distributions of E_{vis}/E_{beam} (a) and P_{bal} (b) for the events passed through selection criteria (1)–(4) at $\sqrt{s}=56$ GeV. The arrows indicate cut values used for this simulations, which are normalized to the integrated luminosity at $\sqrt{s}=56$ GeV.

shows the number of events after applying each selection criterion. These multihadronic candidates were used for the analysis of a heavy quark search which appears in Chapter 5.

4. Measurement of the R-ratio

The R-ratio is calculated experimentally as

$$R = \frac{N_{\text{obs}} - N_{\text{BG}}}{L\ A\ \sigma_{\text{point}}}, \tag{1}$$

where N_{obs} and N_{BG} are the number of observed hadronic events and background events, respecively. L is the integrated luminosity, and A is the overall acceptance. The point-like cross section, σ_{point}, can be expressed as

$$\sigma_{\text{point}} = \frac{4\pi\alpha^2}{3\ s} = \frac{86.9\,[\text{nb}\cdot\text{GeV}^2]}{s}.$$

4.1. Total hadronic cross sections

The hadron production in e^+e^- annihilation is described by the standard $SU(3)\otimes SU(2)\otimes U(1)$ model. The hadron production can be divided into three stages as shown in Figure 8. At first, a quark pair is produced through a photon or a neutral weak boson in e^+e^- annihilation. This process is well described by the electroweak theory. Secondly, one or more gluons can be emitted from quarks. This process can be described by the perturbative approach of the QCD [13]. In the final stage, produced partons, namely gluons and quarks, fragment into hadrons. Since the formation of jets is a complex process through the strong interaction, various models have been proposed to describe the formation of jets.

In the lowest order of the electroweak interaction, the normalized cross section R with the first order QCD corrections is described as follows [14]:

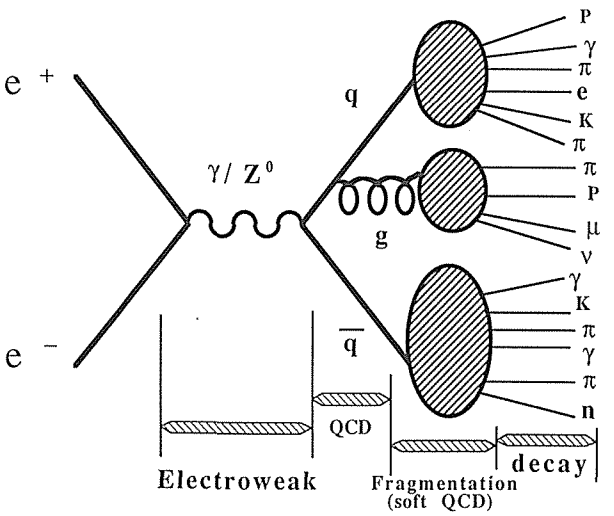

Figure 8 Suchematic diagram for the hadron production in e^+e^- annihilation.

$$R=3\sum_f\left\{\frac{\beta(3-\beta^2)}{2}\left(1+C_1^V\frac{\alpha_s}{\pi}\right)C_{VV}+\beta^3\left(1+C_1^A\frac{\alpha_s}{\pi}\right)C_{AA}\right\}, \quad (2)$$

where

$$C_{VV}=Q_f^2-2Q_fv_ev_fRe[\chi(s)]+(v_e^2+a_e^2)v_f^2|\chi(s)|^2,$$

$$C_{AA}=(v_e^2+a_e^2)a_f^2|\chi(s)|^2,$$

and

$$\chi(s)=\frac{1}{(2\sin 2\theta_W)^2}\frac{s}{s-m_Z^2+i\Gamma_Zm_Z}, \quad (3)$$

Here, the summation extends over all quark flavors whose masses are less than the beam energy. The vector and axial vector couplings of electrons and quarks, v_e, v_f and a_e, a_f, are defined as follows:

$$v_e=-1+4\sin^2\theta_W, \qquad a_e=-1,$$

$$v_{u,c}=+1-(8/3)\sin^2\theta_W, \qquad a_{u,c}=+1,$$

$$v_{d,s,b}=-1+(4+3)\sin^2\theta_W, \qquad a_{d,s,b}=-1.$$

The electroweak mixing angle, $\sin^2\theta_W$, is defined by the ratio of masses of weak bosons as

$$\sin^2\theta_W\equiv 1-\left[\frac{m_W}{m_Z}\right]^2. \quad (4)$$

The dependence on quark masses is included in equation (2) through the quark velocity, β. The QCD correction factors, C_1^V and C_1^A are also the functions of β [13, 14] and they approach to unity as α_s increases. The second order QCD correction [34] is less than 0.2% in the total cross section. The strong coupling constant, β, is given by the secod order QCD [35]. A value of the QCD scale parameter, Λ, is taken to be as $\Lambda_{\overline{MS}}=610$ MeV [10] in the $\overline{MS}$ scheme, and in this case α_s is equal to 0.15 at $\sqrt{s}=56$ GeV.

4.2. Acceptance

The overall acceptance, A, is calculated from the ratio of the accepted cross section which includes the initial photon radiation to the lowest order cross section. It can be calculated as $A=\varepsilon(1+\delta)$ by means of Monte Carlo methods. Here, the detection efficiency of multihadronic events, ε, is defined by the ratio of the number of the accepted events to that of the events generated by a Monte Carlo program. In this case, the radiative correction factor, $(1+\delta)$, is calculated as the ratio of the cross section of generated events to the lowest order cross section.

4.1.1. Radiative correction

The radiative correction of $O(\alpha)$ was evaluated by a complete electroweak calculation according to Shimizu et al. [36]. The total cross section of the hadron production

including the photon emission process is calculated from all possible diagrams of the electroweak interaction up to the order of α^3. In addition to the photonic correction, the vertex correction by the weak bosons, and the self energy correction of weak bosons are taken into account. The contributions due to the quark masses and the width of Z^0 are also included in the calculation. The radiative correction factor $(1+\delta)$ is obtained as a ratio of this total cross section to the lowest order cross section given by the equation (2).

The input parameters of this calculation are α, G_F, m_Z, Γ_Z, the Higgs boson mass, and quark masses. Because the minimal electroweak theory has three free parameters besides the masses of fermions and the neutral Higgs, the electroweak mixing angle is related to G_F, m_Z and α through the following equation:

$$m_Z^2=\frac{\pi\alpha}{G_F\sqrt{2}\,\sin^2\theta_W\,\mathrm{con}^2\theta_W(1-\Delta r)}. \tag{5}$$

In the lowest order of the electroweak theory, the Δr is equal to zero, but Δr is not negligibly small at the next order calculation. The Δr was calculated from the all $O(\alpha^3)$ diagrams of the muon decay, by which the Fermi coupling constant G_F was determined precisely, and it was found to be $\Delta r=0.07$ [37]. The calculation of the Δr slightly depends on the top quark mass, the Higgs mass, and the Z^0 mass. Finally, the electroweak mixing angle was calculated to be $\sin^2\theta_W=0.225$ by using the following parameters: $\alpha=1/137.04$, $m_Z=92.6$ GeV/c^2, and $G_F=1.166\times10^{-5}$ [GeV/c^2]$^{-2}$ [38]. The top quark mass and the Higgs boson mass were chosen to be 50 GeV/c^2 and 100 GeV/c^2, respectively. In this case, the W boson mass was calculated to be 8.15 GeV/c^2 from the equation (4). The total width of Z^0 is calculated to be $\Gamma_Z=2.5$ GeV/c^2 by the electroweak theory, but the result is not sensitive to this value.

The calculation of the hadronic cross section is divided into two parts: the calculation for the radiative process, $e^+e^-\to q\bar{q}$, and the calculation for the non-radiative process, $e^+e^-\to q\bar{q}$. In the calculation for the radiative process, the minimum energy of radiated photons is set to be 100 MeV to avoid the infrared divergence. This infrared divergence can be canceled by the divergence in the vertex correction diagram of the non-radiative process. Therefore, the cross section of the non-radiative process should include the contribution of the radiative process with the photon of smaller than 100 MeV, and the total cross section including both the radiative and the non-radiative processes is free from this infrared divergence. In addition, the maximum energy of photons in radiative process is restricted so that the invariant mass of a hadronic system, $\sqrt{s'}$, can exceed the sum of quark masses by more than 1 GeV. The invariant mass of the hadronic system is related to the energy of the radiated photon, E_γ, as $s'=2\times(E_{\mathrm{beam}}-E_\gamma)\times E_{\mathrm{beam}}$. Roughly speaking, the cross section of the hadronic events with a radiative photon of energy E_γ is a product of two parts: the probability of photon radiation, which is proportional to E_γ^{-1}, and the total hadronic cross section of the remained e^+e^- system, which is proportional to s'^{-1}. For both radiative and non-radiative processes, the cross sections are calculated numerically by using the BASES program [39].

As a result, the radiative correction factor, $1+\delta$, was calculated to be 1.379 at $\delta=55$

GeV and 1.371 at 56 GeV. The parameter values used in the calculations were the same as shown above. These calculations depend on the cut-off value of the maximum photon energy, since the total hadronic cross section increases steeply as the photon energy approaches to the beam energy.

4.2.2. LUND Monte Carlo program

Monte Carlo simulations were performed to study multihadronic events. In this analysis, two types of the LUND Monte Carlo programs were used to generate multihadronic events: JETSET version 5.3 and JETSET version 6.3 [40]. The major difference between these two programs is the QCD calculation used to generate partons in e^+e^- annihilation. In JETSET 5.3, partons are generaed according to the QCD matrix elements calculated up to $O(\alpha_s^2)$ [41]. On the other hand, partons are generated by the parton shower model with a leading log approximation of the QCD [42] in JETSET 6.3. The difference between two models appears in the fraction of four and more jets. The parton shower model in JETSET 6.3 tends to have a larger jet multiplicity. In both programs, the string fragmentation scheme [43] is adopted for the hadronization process.

The full electroweak calculations of the hadronic cross section described in Section 4.2.1 were applied in the LUND programs. Radiated photons are generated according to these calculations by using the SPRING program [39] and then the hadronic system is generated by using the LUND programs. However, the angular distributions of generated quarks and gluons are calculated by the lowest order electroweak interactions and QCD interactions. The major difference between the lowest order calculation and the order of α^3 calculation appears only in the forward-backward charge asymmetry. Therefore, this difference does not affect the R-ratio.

Most of groups at PEP and PETRA tested these LUND models. They found that the LUND models simulated real data very well [44–46]. Nominal values of parameters used in the LUND programs for this analysis are listed in Table 1. The values for JETSET 5.3 were optimized for our data at $\sqrt{s}=52$ GeV and the value for JETSET 6.3 were the same as those used by the MARK II group [46].

Table 2. Parameters of the LUND Monte Carlo programs

JETSET 5.3		JETSET 6.3	
parameter	value	parameter	value
a	1.00	a	0.45
b	0.63	b	0.90
σ_q	0.37 GeV	σ_q	0.33 GeV
Λ_{QCD}	0.40 GeV	Λ_{QCD}	0.40 GeV
Y_{min}	0.02	Q_0	1.0 GeV

4.2.3. Detector Monte Carlo program

A detector Monte Carlo program which simulates responses of the actual VENUS detector is called as VMONT. The VMONT program accepts momentum vectors of final particles in a hypothetical event which is generated by a event generator and then the VMONT produces an output event data which has the same format as the format of real data.

Decays of $\pi^{\pm}$, $K^{\pm}$, $K^0{}_L$ and $\mu^{\pm}$ are included in the VMONT. The position of the decay vertices are calculated even for short life particles, such as $K^0{}_S$, Λ and D mesons, as well as long life particles. The time of flight is also calculated in the VMONT program.

The multiple Coulomb scatterings, energy losses, nuclear interactions, and electromagnetic cascade showers in the detectors are simulated on the actual geometry and materials coded in the VMONT program. Electromagnetic showers in the calorimeters originating from electrons and/or photons are simulated by the EGS program [47]. By basing on the obtained information from the EGS, the responses of calorimeters are calculated. The calo rimeter response for hadrons and muons are also calculated on the basis of the beam test data.

The chamber responses are simulated by using the relation between the drift time and the drift length. The resolution of each detectors are also taken into account. The simulation of detector responses is tuned up from a study on actual responses of detectors. In addition, the VMONT can incorporate simulations of the hardware trigger systems.

4.2.4. Detection efficiency

The detection efficiency of multihadronic events was estimated by means of Monte Carlo simulatons. The selection criteria for multihadronic events (see Section 3.2) were applied to simulated data in the exactly same way as to real data in order to estimate the detection efficiency.

The trigger efficiency was also estimated by examining the trigger conditions for simulated data. The efficiency was found to be more than 99.8% for multihadronic events which satisfy the criteria for the multihadron selection. The trigger inefficiency caused by the detector inefficiency and/or the trigger logic failure was estimated by studying the redundancy of the trigger conditions using the real data. Most of real events passed through the selection criteria were triggered by several types of the event triggers. There was no events triggered by only one kind of trigger and only 1% of events were triggered by two kinds of triggers. Thus our trigger scheme had a sufficient redundancy for multihadronic events. Here, we assumed that the inefficiency of each event trigger would be 1% at most because the events triggered by two kinds of triggers may have occurred due to any trigger failure. In this case, the probability that three kinds of triggers would fail simultaneously was estimated to be less than 1×10^{-6} and it was negligibly small.

In order to justify the detection efficiency obtained from Monte Carlo simulations, the consistencies between the Monte Carlo calculation and the real data for various distributions of observed quantities were examined. The distributions of quantities used

in the event selection are shown in Figure 9 for the real data and the Monte Carlo simulations. Sample events in each distribution were selected through the multihadron selection criteria except for the criterion in which that quantity was used. For example, the events in the distribution of the number of good tracks (Figure 9 (b)) were selected through criteria (1), (3)-(6) in Section 3.2. The distribution of the number of good tracks

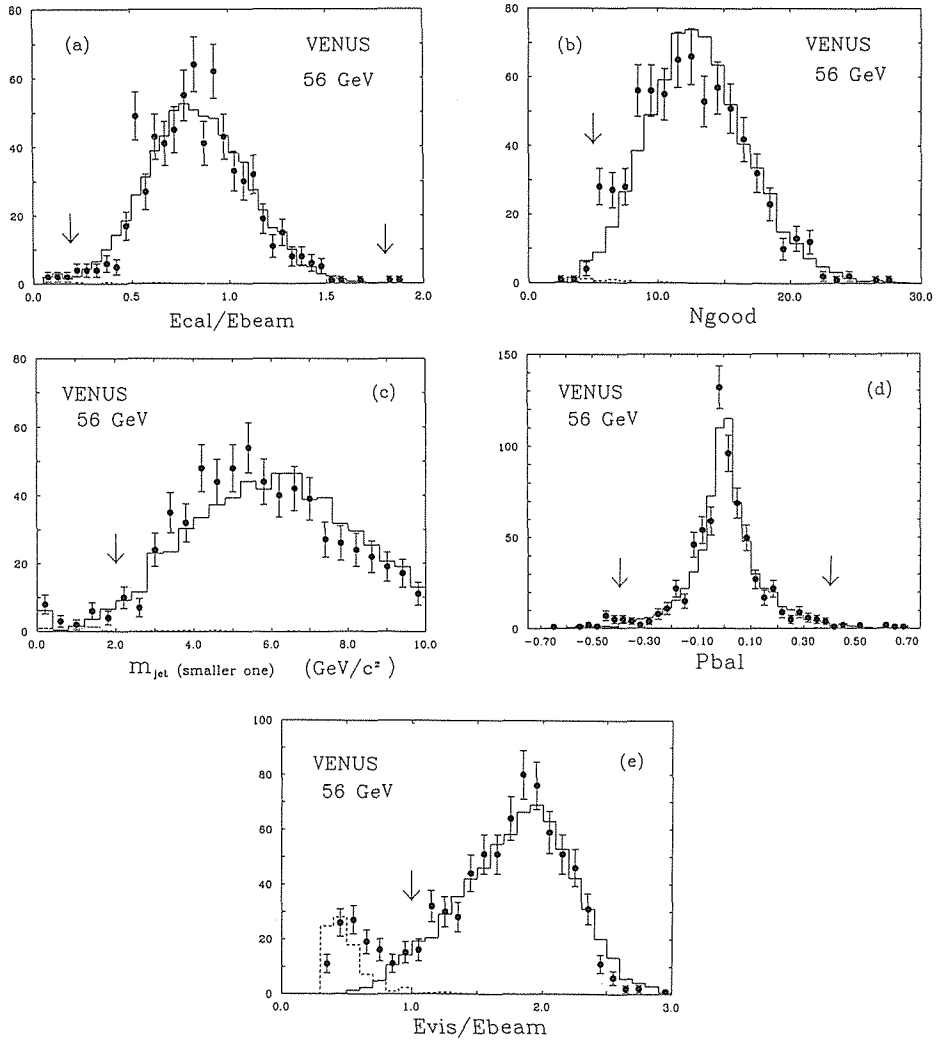

Figure 9 Distributions of the calorimeter energy E_{cal}/E_{beam} (a), the number of good tracks N_{good} (b), the smaller jet mass m_{jet} (c), the longitudinal momentum balance P_{bal} (d), and the total visible energy E_{vis}/E_{beam} (e). The filled circles with error bars show the data at $\sqrt{s}=56$ GeV, where the error bars show the statistical errors only. The histograms show the results from the Monte Carlo simulations: the solid line shows the multihadronic events and the dashed and the dotted lines show the two-photon and the τ pair events, respectively. They are normalized by the integrated luminosity at $\sqrt{s}=56$ GeV. The arrows indicate the cut positions used in the selections for the hadronic events described in Section 3.2.

for the Monte Carlo simulation was slightly larger than that for the real data. By shifing the Monte Carlo distribution so that the mean value of the number of good tracks coincided with that of the real data, the detection efficiency varied by 0.7%. This variation was adopted as one of systematic errors in the detection efficiency. For other distributions, the data and the Monte Carlo Calculations were in good agreement with each other. The systematic error due to a small discrepancy between the Monte Carlo calculation and the data was estimated by studying the cut dependence on the R-ratio. The cut values of $E_{\rm cal}$ and invariant mass were sufficiently safe and hardly affected the detection efficiency. Systematic errors in the detection efficiency due to $E_{\rm cal}$ cut and invariant mass cut were estimated to be 0.4% and 0.3%, respectively. On the other hand, the cut value of the visible energy and the longitudinal momentum balance were much more sensitive to the detection efficiency in comparison with other cut values. Systematic errors in the detection efficiency were estimated to be 0.7% for both cuts.

The difference of the detection efficiency due to the QCD calculations was small. By comparing calculation using the parton shower model (JETSET 6.3) with the matrix element calculation (JETSET 5.3), the difference of the detection efficiency was found to be only 0.3%. On the other hand, by changing the fragmentation parameters to the values of other groups [44–46], a systematic uncertainty due to this origin was found to be 1.1%.

At the 55 GeV run, the gain of the liquid argon calorimetes was varied for the detector study. This gain variation affected the trigger and detection efficiencies. The systematic error due to the gain shift was estimated to be 0.5%.

As a result, the detection efficiency and its systematic uncertainties were calculated to be $\varepsilon=71.5\pm1.9\%$ at $\sqrt{s}=55$ GeV and $70.7\pm1.8\%$ at 56 GeV. Here, all possible systematic errors are added in quadrature.

The overall acceptance, A, is calculated as $A=\varepsilon(1+\delta)$ from obtained values of ε and δ. As shown in Section 4.2.1, the radiative correction strongly depends on the cut-off value of the maximum photon energy. The events with a hard photon emission, however, is hardly detected and thus the overall acceptance does not depend on the cut-off value so much. In most of the events with a hard photon emission, the emitted photon escapes along the beam pipe and is not detected. In this case, the total visible energy becomes small and the longitudinal momentum balance gets worse. Moreover, even if a hard photon hits the calorimeters, an invariant mass in the hemisphere which includes the photon becomes small and the event is rejected by the jet mass cut.

As a result, we obtained $A=0.987\pm0.033$ at $\sqrt{s}=55$ GeV and $A=0.970\pm0.032$ at 56 GeV. The systematic errors in A include the errors in the detection efficiency and 2.1% uncertainty due to the calculation of the radiative correction which mainly comes from the dependence on the cut-off value in the calculation.

4.3. Background contaminations

There were several kinds of background processes in the multihadronic candidates: Bhabha scattering, two-photon processes and tau-pair production. The selection criteria in Section 3.2 were sufficiently stringent so that the number of background events surviving after the cuts were quite small. The contamination of background processes

were studied by the Monte Carlo simulations as will be explained below. Their results are summarized in Table 3. The total of the background contamination was estimated to be $0.5\pm0.2\%$.

4.3.1. Tau-pair production

The pair production of τ leptons which decayed into hadrons is one of background events in the multihadronic candidates. The selection criteria (2) and (4) in Section 3.2 are effective to eliminate these τ-pair events which have very narrow jets with low charged multiplicity. The reduction ratio due to the event selection was estimated by Monte Carlo simulations of τ-pair events. The decay branching ratio into one charged track and that into three charged tracks are 86.5% and 13.4%, respectively [38]. Thus, among the τ-pair events the number of events which had more than 4 charged tracks was very small, and the events which survived after selection criteria (1) and (2) were found to be only 2.4%. About 55% of surviving events had more than 4 charged tracks from the τ-decay and the remainder had at least one track from the photon conversion. In addition, the selection criterion (4) in Section 3.2 is more stringent to cut out the τ-pair events. Figure 10 shows the distributions of invariant masses in both hemispheres for the τ-pair events of the Monte Carlo simulation. The invariant masses are less than 2 GeV/c^2 for most of the τ-pair events. As a result, remaining events under the selection criteria (1), (2), (3), and (4) were found to be $0.16\pm0.08\%$ of the total τ-pair events. The error mainly came from the uncertainties in the branching ratio of τ-decay, especially $Br(\tau\rightarrow 5$ charged) and $Br(\tau\rightarrow 3$ charged$+$some γ's).

Table 3. Backgrounds in the hadronic events at $\sqrt{s}=56$ GeV

	selection criteria (1)–(4)	selection criteria (1)–(6)
τ-pair production	0.17 ± 0.08	0.16 ± 0.08
Two photon hard scattering	17.1 ± 1.2	3.1 ± 0.7
Two photon low Q^2 processes	(92.2)*	<1.0
Bhabha scattering	0.26 ± 0.12	0.26 ± 0.12
total		3.6 ± 1.2

* Estimated number of events from the observed events in the range of $0.4<E_{\rm vis}/E_{\rm beam}<1.0$. (see text)

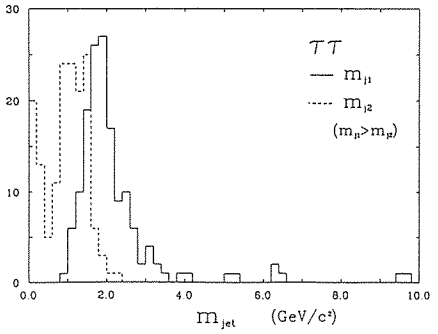

Figure 10 Distributions of the invariant masses in both hemispheres for the Monte Carlo simulation of the τ pair events. The solid and dashed histograms represent the larger and the smaller jet mass, respectively.

The total production cross section of the τ-pair production was calculated to be 39.4 pb at $\sqrt{s}=56$ GeV by using the calculation with a radiative correction of $O(\alpha)$ [43]. Therefore, the background contribution from the τ-pair production was estimated to be $N_{BG}=0.15\pm0.08$ at $\sqrt{s}=55$ GeV and 0.33 ± 0.17 at 56 GeV, respectively.

4.3.2. Two-photon Processes

The hadron production through the two-photon processes (i.e. $e^+e^-\to e^+e^-+$ hadrons) would be the most serious background. The selection criteria (5) and (6) in Section 3.2, especially the visible energy cut, were effective to reduce the background contamination from these two-photon processes. A scatter plot in E_{vis}/E_{beam} and P_{bal} is shown for the data at $\sqrt{s}=56$ GeV and same plots for the Monte Carlo simulatons of the two-photon events and the multihadronic events are also shown in Figure 11. Two-photon events could be characterized by a relatively low visible energy and/or a large missing momentum along the beam direction.

In the Monte Carlo calculations, two types of models for the hadron production through the two photon processes were used to estimate the background contamination; a hard scattering model for high Q^2 processes and a vector-dominance model for low Q^2 process [49].

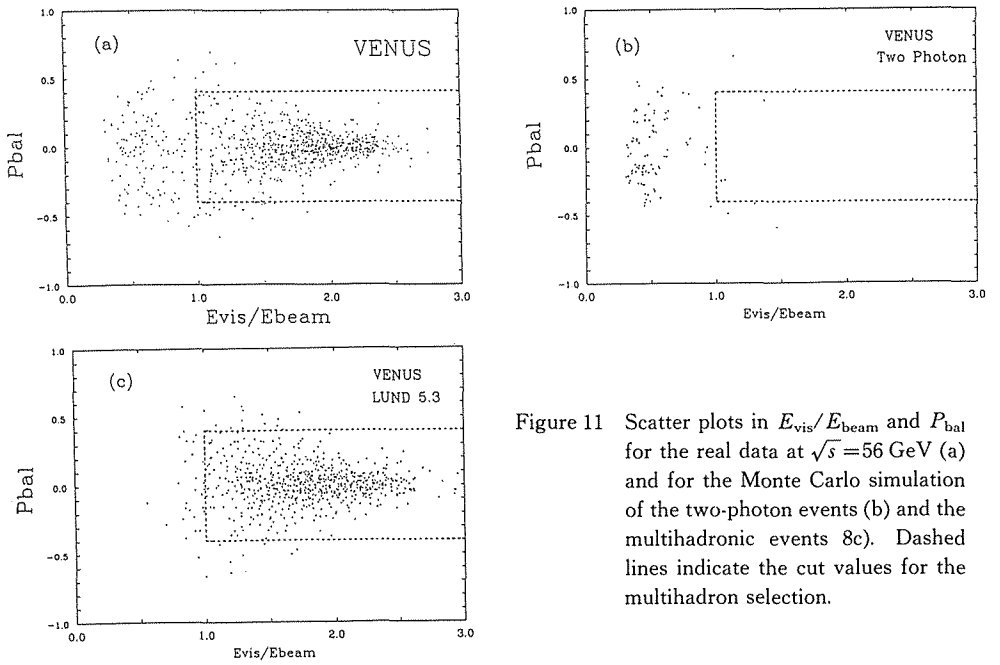

Figure 11 Scatter plots in E_{vis}/E_{beam} and P_{bal} for the real data at $\sqrt{s}=56$ GeV (a) and for the Monte Carlo simulation of the two-photon events (b) and the multihadronic events 8c). Dashed lines indicate the cut values for the multihadron selection.

The vector-dominance hypothesis assumes that photons interact via vector mesons, predominantly ρ mesons, which in turn produce hadrons. The cross section is given by the convolution of the photon-photon cross section with the two-photon luminosity function. The two-photon luminosity function is calculated according to the Weizaker-Williams approximation and the total photon-photon multihadronic cross section, $\sigma_{\gamma\gamma}$, is predicted to be [49, 50]

$$\sigma_{\gamma\gamma}=\left[240+\frac{270}{W_{\gamma\gamma}}\right]F_{\mathrm{GVDM}}(Q^2) \quad [\mathrm{nb}]. \tag{6}$$

where $W_{\gamma\gamma}$ is the center-of-mass energy of the hadronic system in units of GeV. F_{GVDM} is a correction factor depending on Q^2. Contributions of ω and ϕ mesons as well as the ρ meson are included in the F_{GVDM}. In the Monte Carlo program, a pair of quarks and scattered electron and positron are generated according to the calculated cross section at the first step. At the next step, quarks fragment into hadrons basing on the string fragmentation scheme of the LUND Monte Carlo program. Here, parameters in the LUND program are modified for two-photon processes.

The background contribution from the low Q^2 two-photon events was estimated in the following way. The normalization of the Monte Carlo calculation based on the vector-dominance model was determined so that the number of the simulated events, which had lower visible energies of $0.4<E_{\mathrm{vis}}/E_{\mathrm{beam}}<1.0$ and satisfied the selection criteria (1), (2), (3), and (4), agreed with the number of the real events. The number of observed two-photon events was about twice of that expected from the Monte Carlo simulation. This disagreement was caused mainly by the imperfection of the simulation of calorimeter responses. The expected number of events strongly depends on values of the calorimeter cut (criterion (1) in Section 3.2) and the energy threshold of the triggers because the two-photon events have a large peak at low deposited energies. This discrepancy did not affect the results since its contribution was very small. The background contributions of the low Q^2 two-photon reaction to the multihadronic samples was estimated to be less than 0.5 and 1.0 for 55 and 56 GeV data, respectively.

On the other hand, a pair of quarks is produced by the QED processes of α^4 order similar to the reaction $e^+e^-\to e^+e^-\ \mu^+\mu^-$ in the hard scattering model. The α^4 QED cross section was calculated numerically by using the BASES program. The radiative correction and the QCD correction were not included in this calculation. For the quark fragmentation model, the string fragmentation scheme of the LUND Monte Carlo program was also used. The hard scattering process was the dominant source of the background in multihadronic samples. The expected number of events was estimated to be $N_{\mathrm{BG}}=1.4\pm0.4$ at $\sqrt{s}=55$ GeV and 3.1 ± 0.7 at 56 GeV, respectively. Uncertainties in the energy calibration and trigger efficiency were the main source of the systematic error.

4.3.3. Bhabha scattering

Bhabha scattering and its radiative processes could be possible background events in the multihadronic samples. Most of Bhabha events were rejected by requiring five good tracks (the criterion (2) in Section 3.2). But very few events had more than 4 tracks due to electromagnetic showers around the beam pipe.

The total calorimeter energy cut, the criterion (3) in Section 3.2, is effective to eliminate such Bhabha events. Figure 12 shows the distribution of $E_{\mathrm{cal}}/E_{\mathrm{beam}}$ for the events with more than one good tracks. The peak of Bhabha events can be seen at $E_{\mathrm{cal}}=2\times E_{\mathrm{beam}}$ and the tail of lower energies are the Bhabha events in which a part of shower energies escape outside the calorimeters. The ratio of the number of events of

$1.5 < E_{cal}/E_{beam} < 1.8$ to that of events of $1.8 < E_{cal}/E_{beam}$ was estimated to be 0.21. The number of events rejected by the criterion (3) was only 7 events at $\sqrt{s} = 56$ GeV. Therefore, the expected number of the background contamination from Bhabha events is 1.5 ± 0.6 in the samples after the total calorimeter energy cut. The invariant mass cut, the criterion (4) in Section 3.2, is also effective to reduce the background contamination of Bhabha events. This cut requires both an electron and a positron to produce electromagnetic showers, because an invariant mass of a hemisphere, which includes only one electron (or positron) track, is very small even if a bremsstrahlung occurs. Figure 13 shows the distribution of the invariant mass in the hemisphere which includes more than one good tracks for the events with E_{cal} of more than $1.5 \times E_{beam}$. The fraction of the events with the invariant mass of more than 2 GeV/c^2 was found to be 0.41 for each hemisphere and thus the reduction factor by the invariant mass cut was estimated to be 0.17.

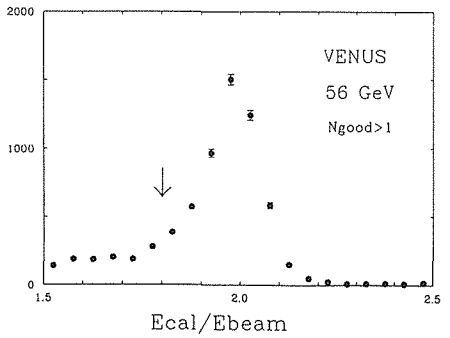

Figure 12 Distribution of the total energy deposit in the calorimeter, E_{cal}/E_{beam}, for the events with more than one good tracks at $\sqrt{s} = 56$ GeV.

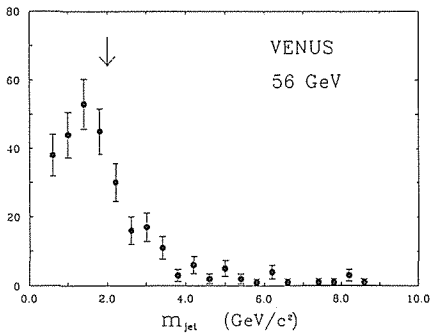

Figure 13 Distribution of the invariant mass in a hemisphere which includes more than one good tracks for the events with E_{cal} of more than $1.5 \times E_{beam}$ at $\sqrt{s} = 56$ GeV. The arrow indicates the cut value.

As a result, the expected number of the background contamination of Bhabha scattering in the multihadronic candidates was estimated to be $N_{BG} = 0.12 \pm 0.05$ at $\sqrt{s} = 56$ GeV and 0.26 ± 0.12 at $\sqrt{s} = 56$ GeV, respectively.

4.4. Luminosity measurements

The Bhabha scattering was measured by the barrel calorimeter and by the end-cap calorimeters. Since the angular distribution of Bhabha scattering in the small-angle region is steeper than that in the large-angle region, even a small uncertainty in the geometrical acceptance of the detector at small angle results the poor precision of the luminosity. Furthermore, it is difficult to study the systematic errors due to the poor tracking capability at the small-angle region. Thus, the systematic error could be larger in the end-cap region. Therefore, the large-angle Bhabha scattering measured by the barrel calorimeter was used to evaluate the integrated luminosity for this analysis, and the small-angle Bhabha scattering measured by the end-cap calorimeter was used to

cross-check the large-angle measurements. The Bhabha scattering measured by the luminosity counters was not used, because the luminosity counter suffered from heavy beam backgrounds by spent electrons.

4.4.1. Central Bhabha scattering

The event which satisfied the following criteria were selected as the Bhabha candidates in the central region [51, 52]:

(1) At least two and at most four good tracks with $P_t>1$ GeV/c were found in the central drift chamber.

(2) At least one back-to-back pair of good tracks with $P_t>1$ GeV/c had the acollinearity angle of less than 10°.

(3) Both tracks of the collinear pair were within $|\cos\theta|\leq 0.743$.

(4) Each track of the pair was associated with a shower cluster in the barrel calorimeter within a cone of 10° around the track, and an energy of the cluster was larger than 1/3 of the beam energy.

There remained 858 events at $\sqrt{s}=55$ GeV and 1861 events at $\sqrt{s}=56$ GeV as the Bhabha candidates, respectively.

The backgrounds from the multihadronic events and the τ-pair production were estimated to be 0.1% and 0.3%, respectively, by the Monte Carlo simulations. The contamination from the double conversion of $\gamma\gamma$ events was estimated to be 0.1% from the study on the conversion probability of photons.

The acceptance was evaluated by a Monte Carlo simulation based on the calculations which included all of the diagrams of electroweak interactions up to the order of α^3 [53, 54]. The contamination from radiative events which included e^+e^- in the final state was estimated to be 1.5% of Bhabha candidates.

The corrections due to the dead lead glass modules (0.7%), failure of the track reconstruction (0.4%), and event loss by bremsstrahlung in the detector materials were taken into account. The correction amounted to 2.4% in total. The trigger inefficiency was estimated to be 0.1% at most.

The major source of the systematic error was the uncertainty in the detector acceptance. It was estimated by changing the cut value of the polar angle of the charged tracks and the acollinearity angle between the tracks. The systematic error in the luminosity measurement was estimated to be 2.6% in total.

As a result, the integrated luminosity was evaluated to be $2.34\pm0.08\pm0.06$ pb^{-1} at $\sqrt{s}=55$ GeV and $5.26\pm0.12\pm0.14$ pb^{-1} at $\sqrt{s}=56$ GeV, where the first errors are the statistical error and the seconds are systematic one.

4.4.2. End-cap Bhabha scattering

The Bhabha scattering measured by the end-cap calorimeters with high statistics was used to cross-check the results of the large-angle Bhabha scattering. The event candidates for the Bhabha scattering in the end-cap region were selected by requiring

that at least one pair of shower clusters in the end-cap calorimeter satisfied the following criteria [52]:

(1) Each cluster energy exceeded 1/3 of the beam energy.

(2) Each cluster was within $0.822 \leq |\cos\theta| \leq 0.968$.

(3) Acollinearity angle between the clusters was less than 10°.

There remained 9106 events at $\sqrt{s}=55$ GeV and 21508 events at $\sqrt{s}=56$ GeV as the Bhabha candidates, respectively.

The background contamination from $\gamma\gamma$ events was estimated to be 1.6% by Monte Carlo simulations according to the calculation up to the order of α^3 [55].

The acceptance was studied by the Monte Carlo simulation based on the same calculation as that used for the central Bhabha events. The uncertainty of the cluster position was the most serious problem to measure the luminosity in the end-cap region. The systematic error in the luminosity was estimated to be 3.9% in total.

As a result, the integrated luminosities obtained from the end-cap Bhabha scattering were $2.20\pm0.02\pm0.09$ pb^{-1} at $\sqrt{s}=55$ GeV and $5.39\pm0.04\pm0.21$ pb^{-1} at $\sqrt{s}=56$ GeV, respectively, where the first errors are the statistical error and the seconds are systematic one. These results are in good agreement with the measurements at the central region within errors.

4.5. Results

The resulting value of R-ratio is given by

$$R=\frac{N_{\rm obs}-N_{\rm BG}}{L\ \varepsilon(1+\delta)\ \sigma_{\rm point}},$$

$$=4.11\pm0.30(\text{statistical})\pm0.18(\text{systematic}) \quad \text{at} \quad \sqrt{s}=55\ \text{Gev},$$

$$=4.83\pm0.22(\text{statistical})\pm0.21(\text{systematic}) \quad \text{at} \quad \sqrt{s}=56\ \text{GeV}.$$

The results of the measurement of the R-ratio using the VENUS detector is summarized in Table 4 together with the previous measurements [17], and the systematic uncertainties in the R-ratio is summarized in Table 5. Since the sources of systema-

Table 4. Results of the R-ratio at the VENUS detector

	50 GeV	52 GeV	55 GeV	56 GeV
R-ratio	$4.4\pm0.5\pm0.4$	$4.7\pm0.3\pm0.5$	$4.11\pm0.30\pm0.18$	$4.83\pm0.22\pm0.21$
$N_{\rm obs}$	96	399	274	681
$N_{\rm BG}$	1.6	6.8	1.7	3.5
ε	0.683	0.678	0.715	0.707
δ	0.32	0.31	0.379	0.371
A	0.902	0.888	0.987	0.970
L(pb^{-1})	0.69	2.90	2.34	5.25

Table 5. Systematic errors in the R-ratio

	point-to-point errors	overall errors
Integrated Luminosity		2.6%
Background contamination	0.2%	
Acceptance	1.8%	2.7%
Radiative correction		2.1%
Monte Carlo statistics	0.7%	
Monte Carlo parameter		1.6%
Monte Carlo model		0.4%
Cut dependence E_{cal}	0.6%	
Cut dependence N_{good}	1.0%	
Cut dependence m_{jet}	0.4%	
Cut dependence P_{bal}	0.7%	
Cut dependence E_{vis}	0.7%	
Trigger efficiency	0.5%	

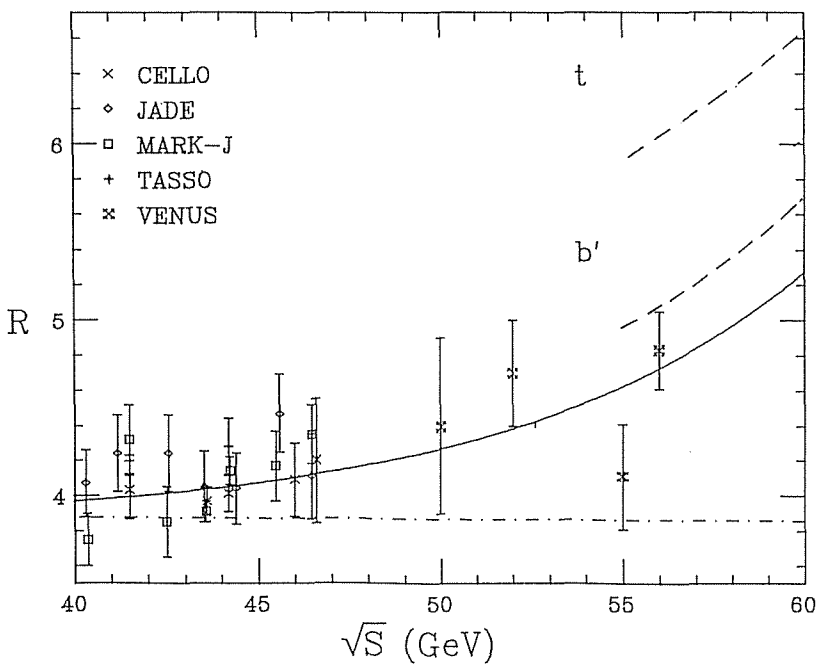

Figure 14 Plot of the present results of the R-ratio together with our data at $\sqrt{s}=50$ GeV and 52 GeV and those measured at PETRA, where the error bars in the figure represent statistical errors only. The solid line indicates the predicted values from the standard model of known five flavor quaks. The dashed lines show the predicted value including the production of the top quarks or the b' quark.

tic uncertainties are presumably independent on each other, the systematic error was determined by adding all uncertainties in the quadrature. In Figure 14 the present results of R-ratio are plotted together with our data at $\sqrt{s}=50$ GeV and 52 GeV [17] and those measured at PETRA energies [10], where error bars in the figure represents statistical error only.

4.6. Discussions

The R-ratio can be predicted by the standard model as the equation (2) in Section 4.1. The predicted values for the known five flavor production are $R=4.53$ at $\sqrt{s}=55$ GeV and $R=4.62$ at $\sqrt{s}=56$ GeV. The electroweak mixing angle is set to be $\sin^2\theta=0.225$ by using the equation (5). The QCD scale parameter is set as $\Lambda_{\overline{MS}}=610$ MeV. There are about 2% of errors in the predicted values because of the ambiguities in m_Z and $\Lambda_{\overline{MS}}$. The measured R-ratio is quite consistent with the predicted value from the standard model with the known five flavor production. The solid line in Figure 14 indicates the predicted values from the standard model of known five flavor quarks.

Assuming that the number of the produced quark flavor is five, it is possible to evaluate the electroweak mixing angle by fitting the equation (2) to the present data at $\sqrt{s}=55$ and 56 GeV. Parameters in the fitting are the mixing angle $\sin^2\theta$ and overall normalization factor f. The Z^0 mass is given by $\sin^2\theta$ by using the equation (5). The fitted value is obtained so as to give the minumum value for the following χ^2 function;

$$\chi^2=\sum_s\left[\frac{R_{\text{theory}}(s)-f\cdot R_{\text{mes}}}{\sigma(s)}\right]^2+\left[\frac{1-f}{\sigma_{\text{norm}}}\right]^2. \tag{7}$$

Here, $R_{\text{theory}}(s)$ and $R_{\text{mes}}(s)$ are the predicted value and the measured value of the R-ratio at the center-of-mass energy of $\sqrt{s}$. The σ_{norm} is the overall normalization error of 3.7% which mainly comes from the systematic error and $\sigma(s)$ is the point-to-point error which mainly comes from the statistical error. The result is $\sin^2\theta_W=0.22\pm0.03$ and the corresponding Z^0 mass is $m_Z=93.0\pm5.0$ GeV/c^2. This value is consistent with the world average [38].

If the top quarks were produced, the R-ratio would give a step rise of about 4/3. The predicted value of the six flavor production obtained from the standard model is $R=6.15$ at $\sqrt{s}=56$ GeV, where the threshold effect due to the top quark mass is neglected (namely $\beta=1$). This predicted value of the "full open top production" is larger by 4.7 standard deviations than the measured value. Thus, the hypothesis of open top quark production can be clearly rejected by the R-ratio alone. In the case of a charge $-1/3$ quark, the predicted value of the full open production is $R=5.15$ at $\sqrt{s}=56$ GeV. This value is larger by only 1.1 standard deviations than the measured value, and the production of the charge $-1/3$ quark could not be rejected by the present results. The dashed lines in Figure 14 show the predicted values of the R-ratios including the production of the top quarks or the b' quark. A detailed analysis of searching for the heavy quarks will be discussed in Chapter 5.

5. Search for heavy quarks

5.1. *Heavy quarks*

Two types of sequential heavy quarks have been searched: a charge +2/3 quark of the third generation (t) and a charge −1/3 quark of the fourth generation (b'). Here, the production of a quarkonium, which is a bound state of quark anti-quark pair, was not taken into the consideration. This analysis was sensitive to the open production of the heavy quarks only.

A heavy quark and its anti-quark are produced through the γ/Z^0 exchange in e^+e^- annihilation. The production cross section of the heavy quarks can be calculated according to the lowest order electroweak interactions through equation (2) of Chapter 5. The total cross section of the heavy quark production strongly depends on the quark mass through the quark velocity β. Roughly speaking, the vector part of the cross section, which is the term including C_{VV} in the equation (2) of Section 4.1, is proportional to β and decreases as the quark mass approaches the beam energy. On the other hand, the axial vector part, which is the term including C_{AA}, is proportional to β^3, and thus the axial part is negligibly small compared with the vector part for the heavy quark as far as its mass is close to the beam energy. The QCD correction factors, C_1^V and C_1^A, rapidly increase as β approaches to zero [13, 14]. The electroweak radiative correction [36] also depends on the quark mass. If heavy quarks are produced at the beam energy close to their mass, the radiative correction factor decreases because the maximum energy of radiated photons decreases.

The heavy quark would decay into light quarks and leptons through weak interaction. The top quark would presumably decay into a bottom quark jet plus light quark jets, or decays into a bottom quark jet plus a charged lepton with a neutrino. The bottom quark, the decay product of the top quark, would decay into a charm quark and then the charm quark would decay into a strange quark, as follows;

$$
\begin{aligned}
t &\rightarrow b + q_1\bar{q}_2(l\nu) \\
&\quad \hookrightarrow c + q_1\bar{q}_2(l\nu) \\
&\qquad \hookrightarrow s + q_1\bar{q}_2(l\nu).
\end{aligned}
$$

Such a cascade chain of weak decays would increase the multiplicity of the final particles in the production of the top quark. The decay of the b' quark would be similar to that of the top quark except that a charm quark would be produced at first instead of a bottom quark.

The heavy quark production can be characterized by its event shape. In the production of ordinary light quarks, that it, u, d, s, c, and b quark, events have a pair of back-to-back jets; final particles from each quark are boosted at a high velocity and concentrate in a narrow cone. A hard gluon can be often emitted, and in this case three jets will be produced in an event plane. On the other hand, particles produced from the heavy quark will be spread in a wide angular region due to the lack of the Lorentz boost, since the velocity of the heavy quark becomes low as the quark mass approaches the beam energy. Moreover, cascade decays of the heavy quark with high Q-values will bring the high multiplicity and the decay products will spread out in whole derections.

Therefore, the event shape of a heavy quark is expected to be spherical. It should be noted that the multi-jets production, such as $e^+e^- \rightarrow q\bar{q}gg$ or $q\bar{q}q\bar{q}$, may also cause the spherically shaped events.

5.2. *Event shape analysis*

An additional cut, $|\cos\theta_T| < 0.7$ (selection criterion (7) in Section 3.2), was applied to the multihadronic event candidates in order to study the event shape. This limitation to the direction of the thrust axis ensures that most of final particles are inside the fiducial volume of the central drift chamber.

In order to describe the event shape in a quantitative way, we have used the sphericity tensor and its eigenvalues. The sphericity tensor, $T_{\alpha\beta}$ is defined by the following equation:

$$T_{\alpha\beta} = \sum_{i,j} \frac{P_\alpha^i P_\beta^i}{|P^i| \ |P^i|} . \tag{8}$$

Here, P_α^i represents the α-th component of a momentum of i-th final particle, and the summation runs over all good tracks and all clusters of energies above 0.2 GeV. Three eigenvalues of the sphericity tensor, which are ordered as $Q_1 < Q_2 < Q_3$ with $Q_1 + Q_2 + Q_3 = 1$, express the event shape; the sphericity is equal to $1.5 \times (1 - Q_3)$ and the eigenvector associated to Q_3 points along the jet axis. Here, Q_1 and $Q_x \equiv (Q_3 - Q_2)/\sqrt{3}$ are used to study the event shape. The Q_1 expresses the thickness along the direction normal to the event plane and the Q_x expresses the spread in the event plane.

Figure 15 (a) and (b) show triangular plots of Q_1 versus Q_x for the data at $\sqrt{s} = 55$ GeV and $\sqrt{s} = 56$ GeV, respectively. The events with two jets concentrate on the right corner and the events with a hard gluon emission spread around the left-lower side of the triangle. The results from the Monte Carlo simulation based on the production of known five flavors are shown in Figure 16 (a) using the LUND Monte Carlo program (JETSET 5.3). On the other hand, spherically shaped events produced from the heavy quarks are expected to be scattered in the left-upper region as shown in Figure 16 (b).

For selecting such spherically shaped events which could result from the heavy quark production, the following cuts were applied to the events which remained after the thrust axis cut (criterion (7)):

$$Q_1 > 0.05 \qquad \text{and} \qquad Q_x < 0.4.$$

These cut values were chosen to keep the detection efficiency of the heavy quarks high enough.

After the cuts for the spherically shaped events, there remained 8 events at $\sqrt{s} = 55$ GeV and 8 events remained also at $\sqrt{s} = 56$ GeV as the candidates for the production of the heavy quarks.

5.3. *Production cross section of heavy quarks*

The production cross section of the heavy quark, such as the top quark and the b' quark, was calculated from the number of spherical events as follows:

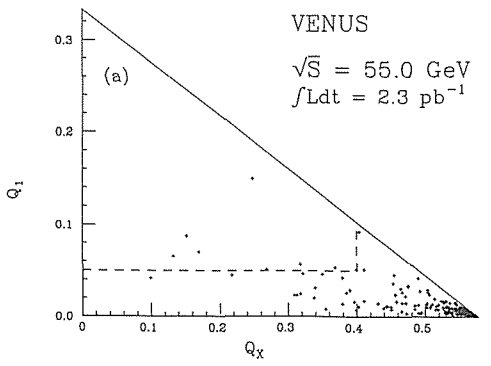

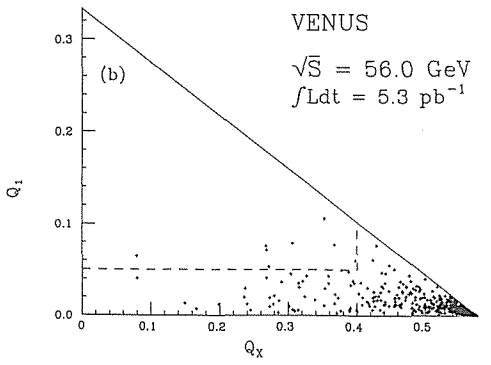

Figure 15 Triangular plots Q_1 versus Q_x for the events passed through the selection criteria (1)–(7) in Section 3.2 at $\sqrt{s}=55$ GeV (a) and at $\sqrt{s}=56$ GeV (b). The dashed lines indicate the cut values for the spherically shaped events.

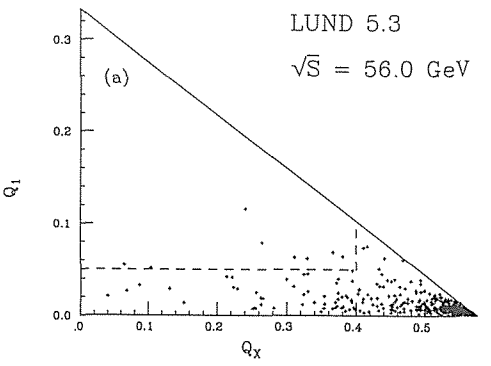

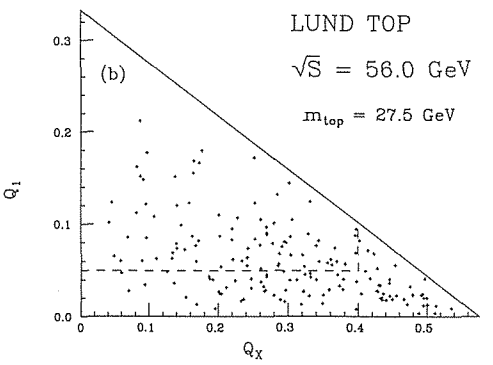

Figure 16 Triangular plots of Q_1 versus Q_x for the Monte Carlo simulations of the production of known five flavors (a) and the production of the top quarks (b). The number of events in the plots are normalized by the luminosity at $\sqrt{s}=56$ GeV. The dashed lines indicate the cut values for the spherically shaped events.

$$\sigma = \frac{N_{sp} - N_{5f}}{\varepsilon L}. \tag{9}$$

Here, N_{sp} and N_{5f} are the number of the observed events and the number of events expected from the five flavor production in the spherical region defined as before, ε is the detection efficiency of a heavy quark, and L is the integrated luminosity.

The expected number of spherically shaped background events from the known five quark production, N_{5f}, was evaluated from the Monte Carlo simulatons. The LUND Monte Carlo programs were used to calculate the contamination from the five flavor production. The calculation of this contamination has systematic uncertainties originated from the model dependence of the Monte Carlo simulations. The fraction of multi-jets events in the parton shower model (JETSET 6.3) is larger than that of the QCD matrix element calculation (JETSET 5.3). Therefore, the number of such spherically shaped events as the backgrounds is rather large for the parton shower

model. The distribution of the event shape also depends on the fragmentation scheme. As a result, the expected numbers of the the background contamination from the five flavor production, N_{5f}, were evaluated to be 3.5 ± 1.6 events at $\sqrt{s}=55$ GeV and 7.9 ± 3.6 events at $\sqrt{s}=56$ GeV, where the systematic errors in N_{5f} were estimated by changing fragmentation parameters and models.

The detection efficiency of the heavy quark production, ε, depends on its mass. The heavy quark will tend to decay into two jets in a back-to-back configuration at its rest frame. In the laboratory frame, final particles are boosted by the quark velocity. The angle between these two jets will become wider as the quark velocity becomes lower. Therefore, the event shape will tend to be spherical and the detection efficiency increases as the quark mass increase. However, the detection efficiency decreases at the mass nearly equal to the beam energy. If heavy quarks are produced almost at rest, each heavy quark will decay into two jets in a back-to-back configuration even in the laboratory frame. In that case, the event topology will be four jets in a plane and can not be spherical.

The Monte Carlo method, in which the LUND Monte Carlo program generated the heavy quark events, was used to estimate the detection efficiency. The detection of the top quark with a mass of 27.5 GeV/c^2 was estimated to be $41.7\pm5.7\%$ at $\sqrt{s}=56$ GeV, where the systematic error was estimated by changing the decay branching ratio, parameters of the fragmentation model, and the radiative correction scheme. For the b' quark, the detection efficiency was estimated to be $27.9\pm2.5\%$ when its mass is equal to 27.5 GeV/c^2.

5.4. Results

As the candidates for the heavy quark production, 8 spherical events were found at $\sqrt{s}=55$ GeV and also 8 events were found at $\sqrt{s}=56$ GeV. The number of spherical events at $\sqrt{s}=56$ GeV is in good agreement with the number expected from the production of five flavors. This agreement was further examined by varying the cut values of Q_1 and Q_x. The number of the observed events is somewhat large at $\sqrt{s}=55$ GeV, but this number is larger by only 1.5 standard deviations than the expected number of events from the five flavors production. If any heavy quarks caused this enhancement, the effect would be more apparent at $\sqrt{s}=56$ GeV because of the increase of the production cross section proportional to β. Therefore, the data at our highest energy of $\sqrt{s}=56$ GeV has been used to obtain the mass limit of the heavy quarks.

As a result, the 95% confidence level upper limit of the cross section of the top quark production has been obtained as follows:

$$\sigma_t<5.6 \text{ pb} \qquad \text{for a top quark with } m_t=27.5 \text{ GeV}/c^2.$$

Here, systematic errors in the detection efficiency, the integrated luminosity, and the background contamination from the light quark productions were linearly summed up in this calculation for setting a conservative upper bound, since these systematic errors might be correlated each other. Figure 17 (a) shows the upper limit of the production cross section as a function of the top quark mass, m_t, together with the theoretical

prediction; the dot-dashed line indicates the cross section which is derived from the calculation including the radiative correction and the threshold effect due to the finite quark mass, and the dashed line indicates the calculation without the quark mass effect. As shown in this figure, the production of the top quarks can be rejected for entire mass range up to 27.5 GeV/c^2. As for the mass range above 27.5 GeV/c^2, the open top picture, where events have jets including "top" mesons, is difficult to be applied and the production of a quarkonium of the top quarks may start to contribute to the hadron production. The production of the quarkonium would not increase spherical events but events with disk shape. Thus, we have obtained the lower mass limit of 27.5 GeV/c^2 at 95% C.L. for the top quark.

As for the b' quark, the upper limit of the production cross section, $\sigma_{b'}$, is calculated to be

$$\sigma_{b'}<8.0 \text{ pb} \qquad \text{for a } b' \text{ quark with } m_{b'}=27.5 \text{ GeV}/c^2.$$

Figure 17 (b) show the obtained upper limit as a function of the b' quark mass together with the prediction. The lower mass limit of 25.6 GeV/c^2 has been obtained at 95% C.L.

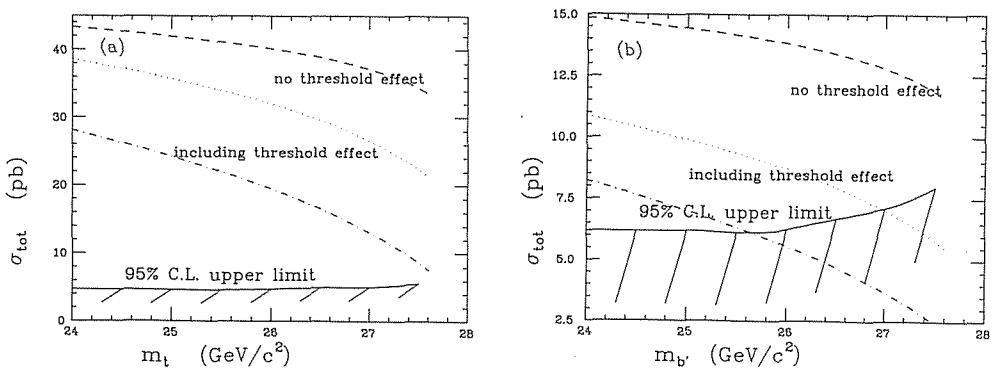

Figure 17 Upper limits of the production cross section of the top quark (a) and the b' quark (b) as a function of the heavy quark mass. The dot-dashed line indicates the expected cross section which is derived from the calculation including the radiative correction and threshold effect due to the quark mass. Whereas, the dashed and the dotted lines indicate the calculation without the quark mass effect, where the dashed line indicates the calculation with $C_1^V=1$ and $C_1^A=1$.

6. Conclusions

We have measured the total hadronic cross section in e^+e^- annihilation using the VENUS detector at TRISTAN, which provides the highest center-of-mass energies at present. The obseved R-ratio are

$$R = 4.11\pm0.30(\text{statistical})\pm0.18(\text{systematic}) \quad \text{at} \quad \sqrt{s}=55 \text{ GeV},$$

$$= 4.83\pm0.22(\text{statistical})\pm0.21(\text{systematic}) \quad \text{at} \quad \sqrt{s}=56 \text{ GeV}.$$

These values are consistent with the predicted values of the known five flavor production obtained by the standard model; the predicted values are $R=4.53$ at $\sqrt{s}=55$ GeV and $R=4.62$ at $\sqrt{s}=4.62$ at $\sqrt{s}=56$ GeV, respectively. From the observed values at $\sqrt{s}=55$ and 56 GeV, we have obtained the weak mixing angle of $\sin^2\theta=0.22\pm0.03$ and the corresponding Z^0 mass of $m_Z=93.0\pm5.0$ GeV/c^2. These values also agree with the world average values of $\sin^2\theta=0.226\pm0.004$ and $m_Z=92.6\pm1.7$ GeV/c^2.

We have searched for the top quark, which is the sixth quark predicted by the standard model. The "full open" production of the top quark is rejected at 95% confidence-level at $\sqrt{s}=56$ GeV by measurements of the R-ratio. From the detailed study of the event shape, the lower mass limit of the top quark is obtained to be 27.5 GeV/c^2 at 95% C.L. We have also obtained the lower mass limit of the b' quark, which is a charge $-1/3$ quark of the fourth generation, to be 25.6 GeV/c^2 at 95% C.L.

As a result, the standard model is quite consistent with our measurement and there is no sign of the production of the heavy quarks. Measurements at higher energies with higher luminosity is needed for further test of the standard model.

Acknowledgements

The success of the experiment is the result of the dedicated effort of all the member of the VENUS collaboration and TRISTAN machine group.

I am most indebted to my supervisor, Kozo Miyake of Kyoto University, for his continual support and guidance through these six years. I would like to thank Takahiko Kondo and Fumihiko Takasaki of KEK for their useful advice to my entire work at KEK. I would also like to thank Katsuya Amako, Junichi Kanzaki, and many other members of the collaboration for a well established foundation of software components.

Special acknowledgments are due Norio Tamura, Yasuo Hemmi, Motomasa Daigo, and Teruo Nakamura for their contributions to construct the time-of-flight counters and the inner chamber. I am also grateful to the members of KEK electronics group under the leadership of Tokio Ohska for their support.

Appendix Time-of-flight counter system

Beam crossing signal (BCS)

In order to know the collision timing precisely, beam pick-up signals from electrodes set in the beam pipe 5 m away from the interaction point are used for the VENUS detector. The beam pick-up signals are shaped and discriminated with the "one flavor beam trigger module" which was developed at SLAC [56]. The output signals from this module is defined as the beam crossing signal (BCS), which is the timing standard for the VENUS detector. The circuit diagram of the beam tigger module is shown in Figure A-1. The timing jitter of the BCS is found to be less than 30 psec but the timing of the BCS signal shifts about 50 psec during each run due to the decrease of the beam current. The temperature coefficient of the BCS timing is found to be about 10 psec/C°and this effect is negligibly small since ambient temperature in

the electronics hut is controlled within $\pm 5C^\circ$.

The BCS from the electrode set on Z-side, which measures the timing of the electron bunch, is used for the timing reference. The timing of the other side signal is measured as a cross-check. Delayed signals of the BCS are used for the fast clear signal (see section 2.10) which is issued 800 nsec before the next collision.

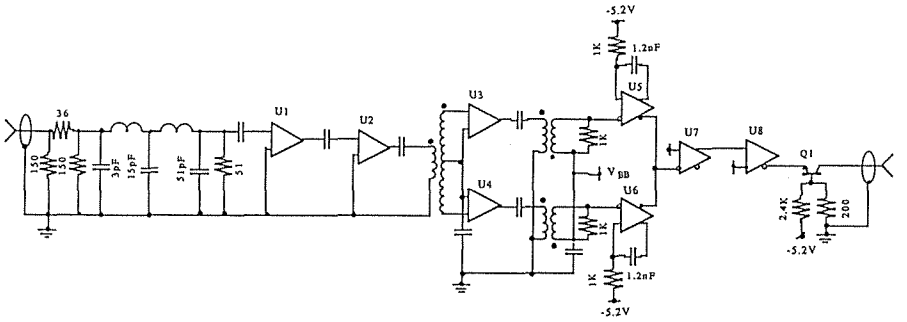

U1-U4 are PLESSY SL532C

U5-U8 are MC10116

Q1 is 2N3960

All capacitor are 0.22μF unless otherwisw specified

Figure A-1 Circuit diagram of the one flavor beam trigger module for the beam crossing signal.

Stucture of the time-of-flight counter system

The time-of-flight counter system [27] consists of 96 plastic scintillators (KYOWA SCSN-23), which surrounds the central drift chamber at a radius of 1.66 m. Each scintillator is 466 cm long, 4.2 cm thick, and 10.8 cm wide. There are 3 mm gaps between adjacent counters. Each counter is wrapped in pieces of black paper and layers of black tape for light shielding. A long acrylic light guide is attached to each end of the scintillator with transparent silicon rubber in order to locate phototubes outside the return yoke. Each phototube is attached to the light guide with silicon rubber. The phototube is surrounded by one layer of μ-metal and two layer of soft iron in order to protect the phototubes against the stray magnetic fields of the solenoidal magnet, typically 150 gauss.

The phototubes are HAMAMATSU R1828 type and they have a good transit time spread of 0.55 nsec. The gain of each phototube was measured by using the americium light pulser before installation. The applied high voltage is adjusted basing on the measured gain so as to achieve equal gain for all phototubes. The high voltage power supply is the LeCroy 4400 system. A high voltage on each phototube is monitored and controlled.

Readout electronics

The schematic diagram of readout electronics system for the time-of-flight counter is shown in Figure A-2. Signals from phototubes are sent to the electronics hut through doubly shielded coaxial cables (35 m long 5D2W). The output signal of each phototube

is sent to a discriminator module and then sent to a charge sensitive ADC and a high resolution TDC, respectively.

The discriminator module called DAB (Discriminator And Buffer module) contains a fast comparator and a fast buffer amplifier for each channel. Each input signal is divided into two and the divided signals are sent to a comparator and a buffer amplifier. The nominal threshold voltage of the comparators is set at -50 mV for all channels.

Output signals from the comparators are fed into TDCs through twisted pair cables. The TDC has a good timing resolution of about 30 psec r.m.s and an excellent stability. Details of the circuit and performance are described in the reference [57]. An essential behavior of the TDC circuit is follows: A constant current is extracted from a capacitor during the time between start and stop signals so that the voltage difference on the capacitor is proportional to the time difference. The voltages before the start signal and after the stop signal are hold by using two sample-and-hold circuits. The voltage difference between them is measured by a 12-bit ADC on the module. Since modules are reset for every 5 μsec by the the fast clear signals, the common stop scheme is employed. The common stop signal is made by delaying BCS. In the common start scheme, the voltages of capacitors without hits would swing from zero to

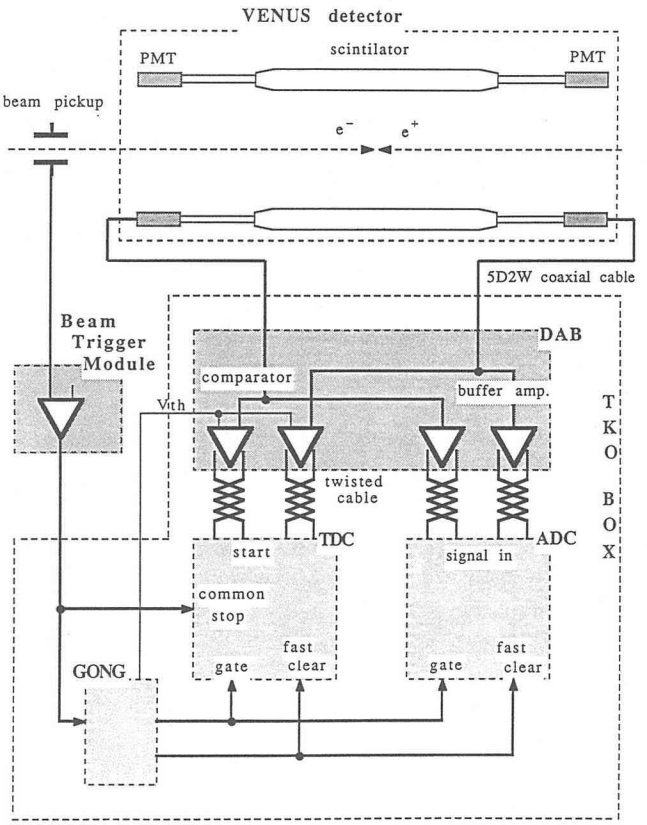

Figure A-2 Schematic diagram of the readout electronics system for the VENUS time-of-flight counter.

the maximum voltage. The number of hits is only a few for each event and thus almost all channels would suffer large voltage swing every 5 μsec. This would worsen the timing resolution significantly. The gate width for the start signal is 120 nsec so that signals which comes about 100 nsec later than the collision timing can be accepted.

Output signals from the buffer amplifiers on the DAB's are fed into charge sensitive ADC's through twisted pair cables in quasi-differential mode. The charge sensitive ADC has a 12-bit resolution and its full scale is 1200 pC. details of its circuit can been seen elsewhere [58]. The gate width is taken to be 150 nsec and the total integrated charge is stored in a hold-capacitor. The two-step sample-and-hold method is also employed and the voltages before and after the gate signal are hold again. The voltage difference between them is measured by a 12-bit ADC in the module. A good stability can be obtained owing to this two-step sample scheme. The pulse height information is mainly used to correct the time slewing. All modules are provided on TKO boxes and digitized data is transferred to memory modules on FASTBUS.

Performance

The calibration of the time-of-flight system has been performed by analyzing the Bhabha events. Velocities of charged tracks in Bhabha events are almost equal to the light velocity and the path length can be well measured with the central drift chamber. Therefore, the time-of-flight of the charged tracks in Bhabha events can be evaluated precisely by using tracking information only. Charged tracks which cause electromagnetic showers in front of the time-of-flight counters are rejected.

The time-of-flight of a charged particle, T_{TOF}, is obtained from the timing information from each phototube, t_{mes}, by the following equation:

$$T_{TOF}=t_{mes}-\frac{l_{pr}}{V}-\frac{a}{\sqrt{Q}}-t_0\,.$$

The second term in the right-hand of the equation is the propagation time of the scintillation light in the counter, where l_{pr} and v are the propagation length and the effective velocity of the light in the scintillator, respectively. The third term indicates the time slewing correction, where Q is the total charge of the signal and a is the correction coefficient, respectively. The timing offset, t_0, indicates the difference of the propagation delay between electronics channels. The effective velocity of light, the time slewing coefficient, and the timing offset are obtained by fitting the data of Bhabha events. The timing resolution in Bhabha events is 200 psec.

The time-of-flight of each charged particle is calculated by using information from phototubes on both sides of the counters for the particle identification. The $\pi/K/p$ separation can be been quite clearly in scatter plots of the velocity versus the momentum of charged tracks in the multihadronic events as shown in Figure A-3.

Laser monitor system

The nitrogen laser is installed to monitor the gain variation of phototubes and to check the stability of electronics. The schematic diagram of the laser monitor system is shown in Figure A-4. Short pulses of ultraviolet light (λ=337 nm) are generated with a

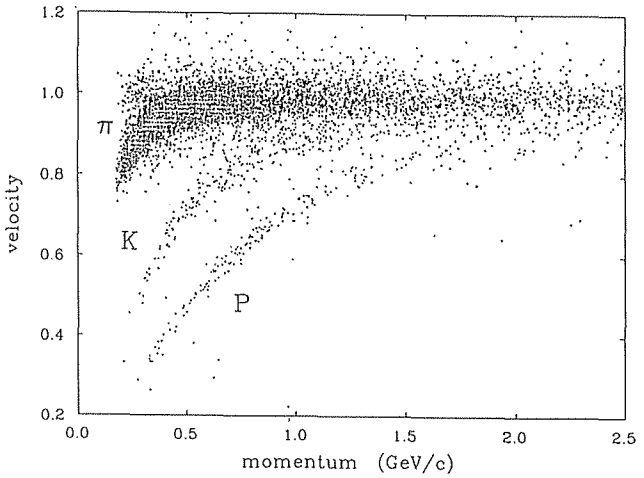

Figure A-3 Scatter plots of the velocity versus the momentum of charged tracks for hadronic events. π, K and p are seen clearly.

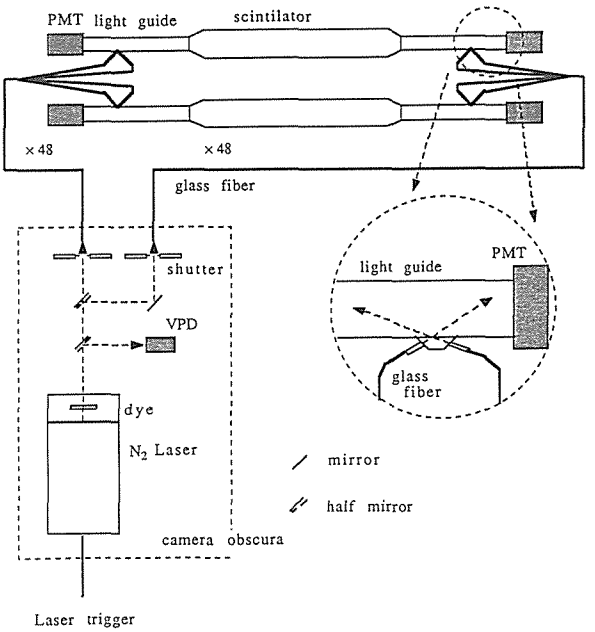

Figure A-4 Schematic diagram of the laser calibration system for the VENUS time-of-flight counter.

nitrogen laser and then are converted to visible light pulses (λ=570 nm) with a dye. Light pulses are distributed to all phototubes through bundles of glass fiber cables. Each side of the time-of-flight counter has a pair of fibers attached on the acrylic light guide. Thus, each counter has four fibers in total. A pair of fibers attached in such a way that one fiber looks toward the phototube on the near side and the other fiber looks toward the phototube on the far side. Therefore, each phototube is flushed through two

light paths; a direct path and a path through a scintillator. Each one of the two paths can be chosen with the optical shutter on each fiber. The precise timing of light pulses is measured with a biplanar phototube (HAMAMATSU R1238U) which has very fast response of less than 100 psec rise time.

The timing information and pulse height information is used to monitor the stability of the electronics system and the phototubes. The timing resolution measured with laser light pulses is less than 100 psec. The light yield of laser pulses, however, changes significantly since the variation of nitrogen pressure, impurities in the nitrogen gas, and spark gap voltage causes the operating condition severely. Since the time slewing for the laser pulses is somewhat different from one for scintillation lights, timing calibration is not performed by using laser pulses.

Reference

[1] M. L. Perl et al., Phys. Rev. Lett., **35** (1975) 1489.
[2] J. J. Aubert et al., Phys. Rev. Lett., **33** (1974) 1404;
J. E. Augustin et al., Phys. Rev. Lett., **33** (1974) 1406.
[3] M. Kobayashi and K. Maskawa, Prog. Theor. Phys. **49** (1973) 652.
[4] S. Herb et al., Phys. Rev. Lett., **39** (1977) 252.
[5] G. Flügge, *Proc. of the 19th Int Conf. on High Energy Physics*, Tokyo (1978).
[6] S. L. Glashow, Nucl. Phys. **22** (1961) 579;
S. Weinberg, Phys. Rev. Lett., **19** (1964) 1264;
A. Salam, in *Elemental Particle Theory, ed. N. Svarthholm* (Almquist and Wiskell, Stockholm, 1968) 367.
[7] UAI Collab., Phys. Lett. **B129** (1983) 273;
UA2 Collab., Phys. Lett. **B129** (1983) 130.
[8] R. Brandelik et al., Phys. Lett. **B86** (1979) 243;
P. Söding, *Proc. EPS Conf. on High Energy Physics*, Geneva (1979).
[9] R. Brandelik et al., Phys. Lett. **B97** (1980) 453.
[10] CELLO Collab., H. J. Behrend et al., Phys. Lett. **B183** (1987) 400;
[11] JADE Collab., B. Naroska, Phys. Rep **148** (1987) 67;
Mark J Collab., B. Adeva et al., Phys. Rev. **D34** (1986) 681;
TASSO Collab., M. Althoff et al., Phys. Lett. **B138** (1984) 441.
[12] MAC Collab., E. Fernandez et al., Phys. Rev. **D31** (1985) 1537;
HRS Collab., D. Bender et al., Phys. Rev. **D31** (1985) 1.
[13] T. W. Appelquist and H. D. Politzer, Phys. Rev. Lett. **34** (1975) 43;
Phys. Rev. **D12** (1975) 1404.
[14] J. Jersak et al., Phys. Rev. **D25** (1982) 1219;
S. Güsten et al., Phys. Lett. **B155** (1985) 185.
[15] ARGUS Collab., H. Albrecht et al., Phys. Lett. **B192** (1987) 245.
[16] C. Albajar et al., Z. Phys. **C37** (1988) 505.
[17] H. Yoshida et al., Phys. Lett. **B198** (1987) 570;
K. Abe et al., J. Phys. Soc. Jpn. **56** (1987) 3763.
[18] TRISTAN project group, KEK Report 86–14, (1987).
[19] J. Iwahori et al., VENUS proposal KEK Report (1983).
[20] H. Saito et al., Nucl. Instr. and Meth. **A270** (1988) 319.
[21] K. Kubo, the Memories of the Faculty of Science Kyoto University, Series of Physics, Astrophysics, Geophysics and Chemistry Vol. **XXXVII** No. 3 (1989) 125.
[22] F. Suekane et al., IEEE Trans. Nucl. Sci. **33** (1986) 73.

[23] M. Ikeno et al., IEEE Trans. Nucl. Sci. **33** (1986) 779.
[24] KEK DA group, "TKO SPECIFICATION", KEK Report 85–10;
T. K. Ohska et al., IEEE Trans. Nucl. Sci. **33** (1986) 98;
H. Kurashige et al., IEEE Trans. Nucl. Sci. **35** (1988) 257.
[25] T. Ohsugi et al., Nucl. Instr. and Meth. **A269** (1988) 522.
[26] R. Arai et al., Nucl. Instr. and Meth. **217** (1983) 81.
[27] Y. Hemmi et al., Jpn. J. of Appl. Phys. **26** (1987) 982;
Y.Yamade et al., the Memories of the Faculty of Science Kyoto University, Series of Physics, Astrophysics, Geophysics and Chemistry Vol. **XXXVII** No. 3 (1989) 1.
[28] R. Arai et al., Nucl. Instr. and Meth. **A254** (1987) 317.
[29] R. Arai et al., Nucl. Instr. and Meth. **A243** (1986) 58;
T. Sumiyoshi et al., Nucl. Instr. and Meth. **A271** (1988) 432.
[30] Y. Asano et al., Nucl. Instr. and Meth. **A259** (1987) 430.
[31] Y. Chiba et al., Nucl. Instr. and Meth. **A269** (1988) 171.
[32] R. Arai et al., Nucl. Instr. and Meth. **A272** (1988) 687.
[33] Y. Nakagawa et al., KEK Report 85–67, (1985).
[34] M. Dine and J. Sapirstein, Phys. Rev. Lett. **43** (1979) 668.
[35] W. E. Caswell, Phys. Rev. Lett. **33** (1974) 244;
D. R. T. Jones, Nucl. Phys. **B75** (1974) 531.
[36] Y. Shimizu et al. Prog. Theor. Phys. **79** (1988) 701.
[37] Z. Hioki et al, Prog. Theor. Phys. **68** (1982) 2134.
[38] Particle Data Group (Review of Particle Properties): Phys. Lett. **B170** (1986) 1.
[39] S. Kawabata, Comput. Phys. Commun. **41** (1986) 127.
[40] T. Sjöstrand, Comput. Phys. Commun. **28** (1983) 229;
T. Sjöstrand, Comput. Phys. Commun. **39** (1986) 347;
T. Sjöstrand and M. Bengtsson, Comput. Phys. Commun. **43** (1987) 367.
[41] R. K. Ellis, D. A. Ross and A. E. Terrano, Nucl. Phys. **B178** (1981) 421;
F. Gutbrod, G. Kramer and G. Schierholz, DESY 83–044 (1983).
[42] M. Bengtsson and T. Sjöstrand, Phys. Lett. **B185** (1987) 435.
[43] B. Anderson, G. Gustafson, G. Ingelman and T. Sjöstrand, Phys. Rep. **97** (1983) 33.
[44] JADE Collaboration, W. Bartel et al., Phys. Lett. **B101** (1981) 129;
Z. Phys. **C21** (1983) 37; Phys. Lett. **B157** (1985) 340.
[45] TPC Collaboration, H. Aihara et al., Z. Phys. **C28** (1985) 31.
[46] MARK II Collaboration, A. Peterson et al., Phys. Rev. **D37** (1988) 1.
[47] W. R. Nelson et al., SLAC-265, December 1985.
[48] F. A. Berends et al., Nucl. Phys. **B202** (1982) 63.
[49] V. M. Bundev et al., Phys. Rep. **C15** (1975) 182;
H. Kolanoski, *Two-Photon Physics at e^+e^- Storage Rings* (Springer-Verlag, Berlin, 1984).
[50] PLUTO Collab., C. Berger et al., Phys. Lett. **B89** (1982) 287;
[51] K. Abe et al., J. Phys. Soc. Jpn. **56** (1987) 3767.
[52] K. Abe et al., *Proc. of the 24th Int Conf. on High Energy Physics*, Munich (1988).
[53] K. Tobimatsu and Y. Shimizu, Prog. Theor. Phys. **74** (1985) 567, **75** (1986) 905, **76** (1986) 334.
[54] S. Kuroda, T. Kamitani, K. Tobimatsu, S. Kawabata and Y. Shimizu, Comput. Phys. Commun. **48** (1988) 335.
[55] J. Fujimoto and M. Igarashi, Prog. Theor. Phys. **74** (1985) 791; J. Fujimoto, M. Igarashi and Y. Shimizu, Prog. Theor. Phys. **77** (1985) 791.
[56] J. L. Pellegrin, private communication.
[57] O. Sasaki et al., IEEE Trans. Nucl. Sci. **35** (1988) 342.
[58] H. Kurashige et al., IEEE Trans. Nucl. Sci. **35** (1988) 1018.